SANDIA REPORT

SAND2014-18127
Unlimited Release
Printed September 2014

Deformation behavior of sub-micron and micron sized alumina particles in compression

Pylin Sarobol, Aaron C. Hall, David A. Urrea, Michael E. Chandross, Jay D. Carroll, Brad L. Boyce, William M. Mook, Paul G. Kotula, Bonnie B. McKenzie, and Daniel C. Bufford.

Prepared by
Sandia National Laboratories
Albuquerque, New Mexico 87185 and Livermore, California 94550

Sandia National Laboratories is a multi-program laboratory managed and operated by Sandia Corporation, a wholly owned subsidiary of Lockheed Martin Corporation, for the U.S. Department of Energy's National Nuclear Security Administration under contract DE-AC04-94AL85000.

Approved for public release; further dissemination unlimited.

Issued by Sandia National Laboratories, operated for the United States Department of Energy by Sandia Corporation.

NOTICE: This report was prepared as an account of work sponsored by an agency of the United States Government. Neither the United States Government, nor any agency thereof, nor any of their employees, nor any of their contractors, subcontractors, or their employees, make any warranty, express or implied, or assume any legal liability or responsibility for the accuracy, completeness, or usefulness of any information, apparatus, product, or process disclosed, or represent that its use would not infringe privately owned rights. Reference herein to any specific commercial product, process, or service by trade name, trademark, manufacturer, or otherwise, does not necessarily constitute or imply its endorsement, recommendation, or favoring by the United States Government, any agency thereof, or any of their contractors or subcontractors. The views and opinions expressed herein do not necessarily state or reflect those of the United States Government, any agency thereof, or any of their contractors.

SAND2014-18127
Unlimited Release
Printed September 2014

Deformation behavior of sub-micron and micron sized alumina particles in compression

Pylin Sarobol[1], Aaron C. Hall[1], David A. Urrea[1], Michael E. Chandross[2], Jay D. Carroll[3], Brad L. Boyce[3], William M. Mook[4], Paul G. Kotula[5], Bonnie B. McKenzie[5], and Daniel C. Bufford[6],

[1]Coatings and Surface Engineering, 01832
[2]Computational Materials and Data Science, 01814
[3]Metallurgy and Materials Joining, 01831
[4]Nanosystems Synthesis/Analysis, 01132
[5]Materials Characterization and Performance, 01819
[6]Radiation-Solid Interactions, 01111

Sandia National Laboratories
P.O. Box 5800
Albuquerque, New Mexico 87185-MS1130

Abstract

The ability to integrate ceramics with other materials has been limited due to high temperature (>800°C) ceramic processing. Recently, researchers demonstrated a novel process, aerosol deposition (AD), to fabricate ceramic films at *room temperature* (RT). In this process, sub-micron sized ceramic particles are accelerated by pressurized gas, impacted on the substrate, plastically deformed, and form a dense film under vacuum. This AD process eliminates high temperature processing thereby enabling new coatings and device integration, in which ceramics can be deposited on metals, plastics, and glass. However, knowledge in fundamental mechanisms for ceramic particles to deform and form a dense ceramic film is still needed and is essential in advancing this novel RT technology. In this work, a combination of experimentation and atomistic simulation was used to determine the deformation behavior of sub-micron sized ceramic particles; this is the first fundamental step needed to explain coating formation in the AD process. High purity, single crystal, alpha alumina particles with nominal sizes of 0.3 μm and 3.0 μm were examined. Particle characterization, using transmission electron microscopy (TEM), showed that the 0.3 μm particles were relatively defect-free single crystals whereas 3.0 μm particles were highly defective single crystals or particles contained low angle grain boundaries. Sub-micron sized Al_2O_3 particles exhibited ductile failure in compression. *In situ* compression experiments showed 0.3μm particles deformed plastically, fractured, and became polycrystalline. Moreover, dislocation activity was observed within these particles during compression. These sub-micron sized Al_2O_3 particles exhibited large accumulated strain (2-3 times those of micron-sized particles) before first fracture. In agreement with the findings from experimentation, atomistic simulations of nano-Al_2O_3 particles showed dislocation slip and significant plastic deformation during compression. On the other hand, the micron sized Al_2O_3 particles exhibited brittle fracture in compression. *In situ* compression experiments showed 3μm Al_2O_3 particles fractured into pieces without observable plastic deformation in compression. Particle deformation behaviors will be used to inform Al_2O_3 coating deposition parameters and particle-particle bonding in the consolidated Al_2O_3 coatings.

ACKNOWLEDGMENTS

The authors would like to acknowledge Jeff Reich for ICP analysis, Michael Rye and Garry Bryant for FIB and TEM sample preparation, Amy Allen and Lisa Deibler for particle size analysis using SEM, James Griego and Mark Rodriguez for XRD, Josh Hubbard and Steven Storch for particle size analysis using a particle counter, Harlan Brown-Shaklee and Deidre Hirschfeld for report review. We are grateful to Paul Clem, Corbett Battaile, Rajan Tandon, and Hy Tran for valuable discussions.

CONTENTS

FIGURES

TABLES

NOMENCLATURE

Å	Angstrom
AD	Aerosol Deposition
AlN	Aluminum Nitride
Al_2O_3	Alumina
at%	Atomic Percent
$BaTiO_3$	Barium Titanate
°C	Degree Celsius
Cu	Copper
E	Young's Modulus (GPa)
EDS	Energy Dispersive X-ray Spectrometry
FF	Force Field
FIB	Focused Ion Beam
fs	Femtoseconds
Ga^+	Gallium Ion
G_C	Strain Energy Release Rate (J/m^2)
GPa	Gigapascal
ICP	Inductively Coupled Plasma Analysis
J/m^2	Joules per square meter
K	Kelvin
K_{IC}	Fracture Toughness (MPa√m)
kV	Kilovolts
$LiCoO_2$	Lithium Cobalt Oxide
$LiMn_2O_4$	Lithium Manganese Oxide
MD	Molecular Dynamics
mm	Millimeters
mN	Millinewtons
MPa√m	Megapascal Square-root meter
m/s	Meters per Second
nm	Nanometer
nm/s	Nanometers per Second
NP	Nano Particle
ns	Nanoseconds
pJ	Picojoules
PNN	Lead Nickel Niobate
PZT	Lead Zirconium Titanate
RT	Room Temperature
s^{-1}	Per Second
s	Second
SEM	Scanning Electron Microscopy
Si	Silicon
Sm-Fe-N	Semarium-Iron-Nitride
SNL	Sandia National Laboratories
s/step	Seconds per Step
STEM	Scanning Transmission Electron Microscopy
TEM	Transmission Electron Microscopy
TiO_2	Titania
XRD	X-ray Diffraction
µg/g	Micrograms per gram
µm	Micrometer
µm/min	Micrometers per Minute
µN/s	Micronewtons per Second

1. INTRODUCTION

In this work, fundamental deformation mechanisms in sub-micron ceramic particles were studied as a basis for particle consolidation (particle-particle bonding) in aerosol deposition (AD). AD is a room temperature (RT) solid-state deposition process. In this novel process, particles are accelerated to high velocity (200-600 m/s) by pressurized gas, impacted, deformed, and consolidated on the substrates at RT under vacuum. High velocity ceramic particles undergo plastic deformation and break up into small crystallites (20-75nm), which bind together [1-3] to form thick films with high deposition rates (10-30 μm/min) [4]. These films have excellent integrity and properties equivalent to or exceeding those of bulk ceramics processed by conventional methods. Deposition of traditional (Al_2O_3, TiO_2, AlN) [2], dielectric ($BaTiO_3$) [4,5], piezoelectric (PZT, PNN) [2,6,7], magnetic (Sm-Fe-N) [8,9] and battery ($LiMn_2O_4$, $LiCoO_2$) [5] ceramic materials has been reported. Traditionally, these ceramic materials were processed at high temperatures, >800°C, limiting ceramic integration with other materials systems. The ability to deposit ceramics using a RT process enables multi-materials (metals, ceramics, polymers) fabrication and device integration.

Although empirical data exist for RT solid-state deposition of ceramics, underlying mechanisms for particle deformation and particle-particle bonding are not understood. Likewise, a large gap exists between the knowledge of ceramic plastic deformation and its role in room temperature consolidation of ceramics particles. Whereas deformation of polycrystalline ceramics may be explained by grain boundary sliding accommodated by slip [10,11] at high temperatures and low strain rate, current literature lacks explanations for deformation at room temperature and high strain rate, applicable to the RT solid-state deposition process. Compression of single crystal sapphire pillars at RT has shown dislocation slip, plastic deformation, and cracking [12]. Similarly, compression of single crystal sub-micron sized Silicon (Si) particles at RT has also shown dislocation activity, plastic deformation, and cracking [13, 14]. Moreover, feature-size-dependent brittle-to-ductile transition in deformation behavior of Si pillars [15] and alumina (Al_2O_3) particles in compression [1] have also been reported in the literature. For Al_2O_3 particles in compression, it has been shown that 'large' particles (>1 μm diameter) fracture into pieces whereas 'small' particles (<500 nm in diameter) plastically deform (Figure 1) [1]. Our hypothesis is that a common underlying mechanism exists for sub-micron sized ceramic particles to plastically deform and bond in RT solid-state deposition processes because similar microstructural characteristics, where particles break up into 20-75 nm sized crystallites were observed for Al_2O_3 (Figure 2), $BaTiO_3$, and PZT solid-state deposited films [5].

Simulation has also been utilized to gain insights into bonding mechanisms. Finite element modeling using the Johnson-Holmquist material model for a single 0.3 μm Al_2O_3 particle impacting a substrate at 150 m/s was performed by Akedo [3]. The conclusions were that the local temperature rise of 500°C was not high enough for sintering (>800°C) and the pressure of 10 GPa was less than that of conventional shock wave synthesis [3]. The effects of local pressure and temperature rise, however, were not investigated experimentally. It may be possible that local pressure during impact may be high enough to create shock-induced amorphization of ceramics [16-18] and that the local temperature rise at the impact interface may be high enough to induce sintering of sub-micron-scale ceramic particles.

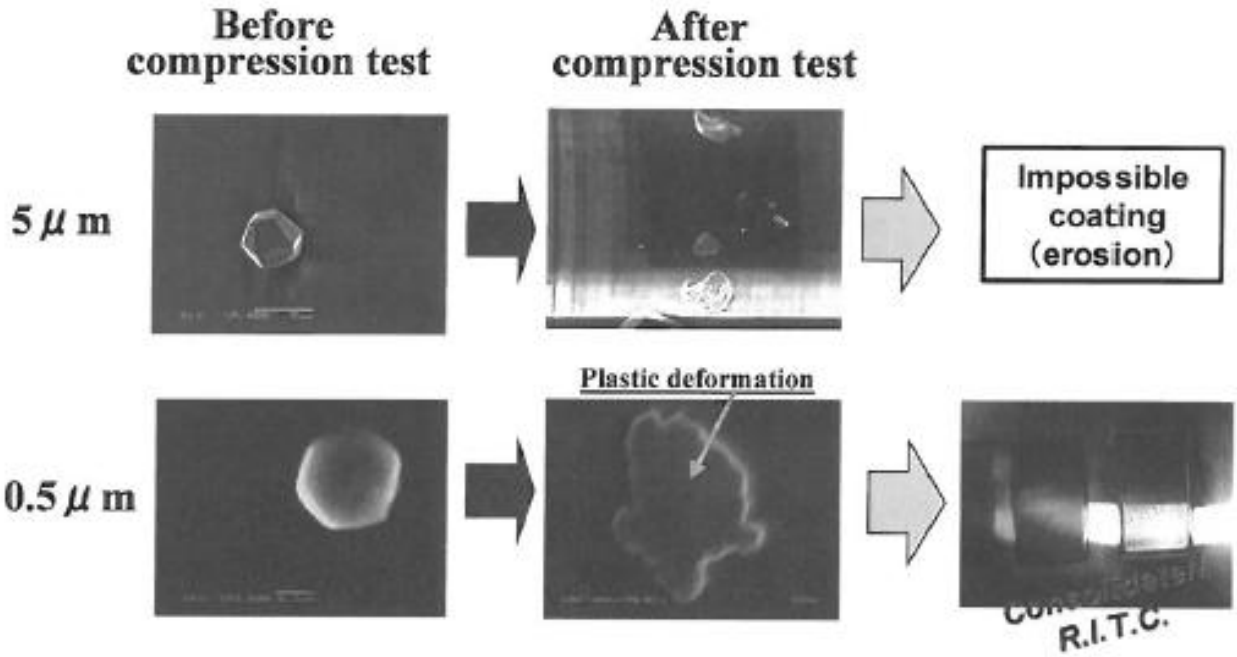

Figure 1: The work by Akedo and Ogiso showing micron-sized alumina particles fractured into pieces and eroded during the deposition whereas sub-micron sized alumina particles deformed during compression and consolidated into coatings during AD [1].

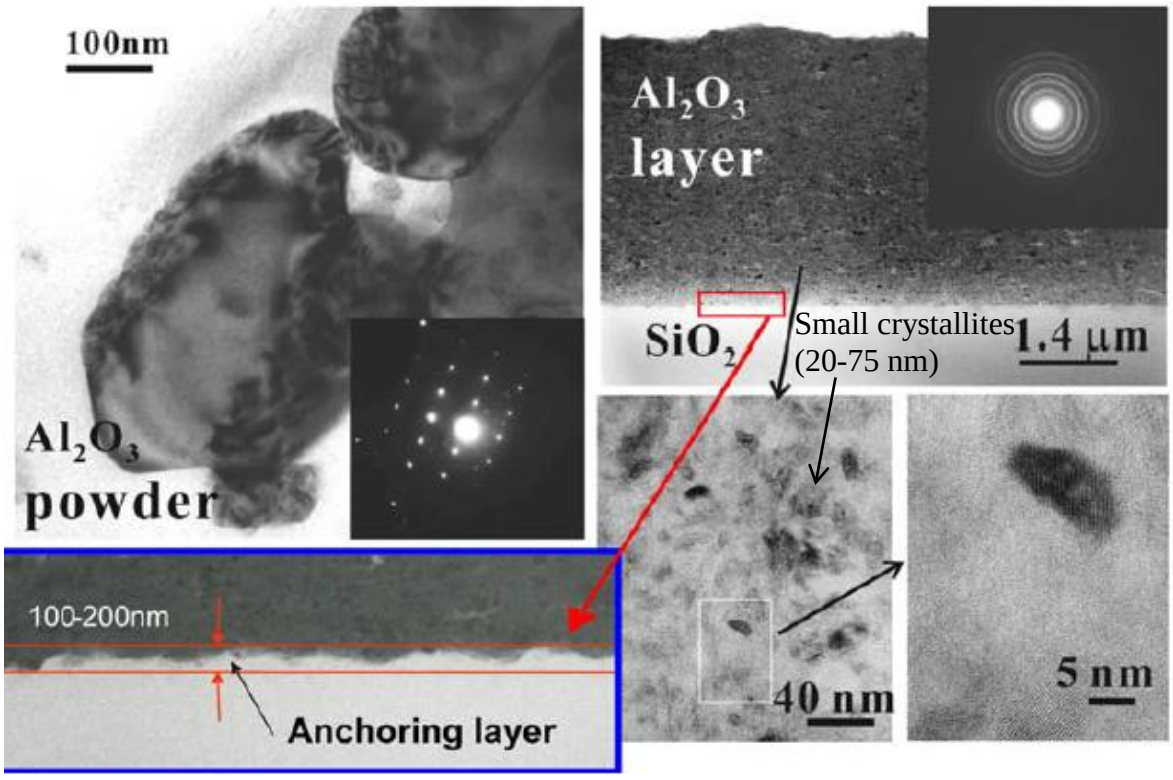

Figure 2: TEM images of Al_2O_3 particles before and after deposition. Small crystallites (20-75 nm) were found inside of the deformed particles after deposition [2].

In order to gain insights into sub-micron and micron sized ceramic particle deformation behaviors, a series of experiments and atomistic simulations were conducted to investigate how the presence/absence of defects in ceramic particles affects deformation behavior. Smaller particles may be relatively defect-free and may be more energetically favorable to deform rather than fracture under compression. The reverse may be true for large particles.

Alumina (Al_2O_3) was selected for this study. Two sets of high purity α-Al_2O_3 particles with nominal sizes of 0.3 μm (AA-03) and 3 μm (AA-3) were obtained from Sumitomo Chemical Co., LTD. Both sets of particles were characterized for morphology, size distribution, possible internal boundaries, purity, and phase. *In situ* compression in the scanning electron microscope (SEM) was performed on both sets of particles to observe the nature of deformation/fracturing behaviors. *In situ* compression in the transmission electron microscope (TEM) was performed only on the electron transparent 0.3μm particles to capture dislocation activities, possible sub-grain formation, and nano-scale fracturing. Load and displacement were recorded during each particle compression.

Atomistic simulations were performed with the goal of understanding features in the load vs. displacement curves during nanoparticle (NP) compression. In particular, load drops in the experimental load vs. displacement curves are often ascribed to either dislocation movement or fracture events in the NPs. Moreover, because molecular dynamics (MD) tracks the motion of individual atoms in a given system, the identification of dislocations, slip planes, and particle fracture is feasible.

2. PARTICLE CHARACTERISTICS

2.1 Particle Morphology and Size Distribution

2.1.1 SEM Image Analysis

The 0.3 µm and 3 µm Al_2O_3 particles were imaged via a Carl Zeiss Supra 55VP, at a working distance of 9 mm, using a 10 kV excitation voltage. The 0.3 µm particle size distribution was analyzed by outlining individual particles in SEM images and making measurements on the outlined particles in the Clemex image analysis software. An example of the image analysis is shown in Figure 3. Over 500 particles were analyzed and particle size distribution was plotted. The 3 µm particle size distribution was analyzed using the automated Oxford Inca Feature analysis suite.

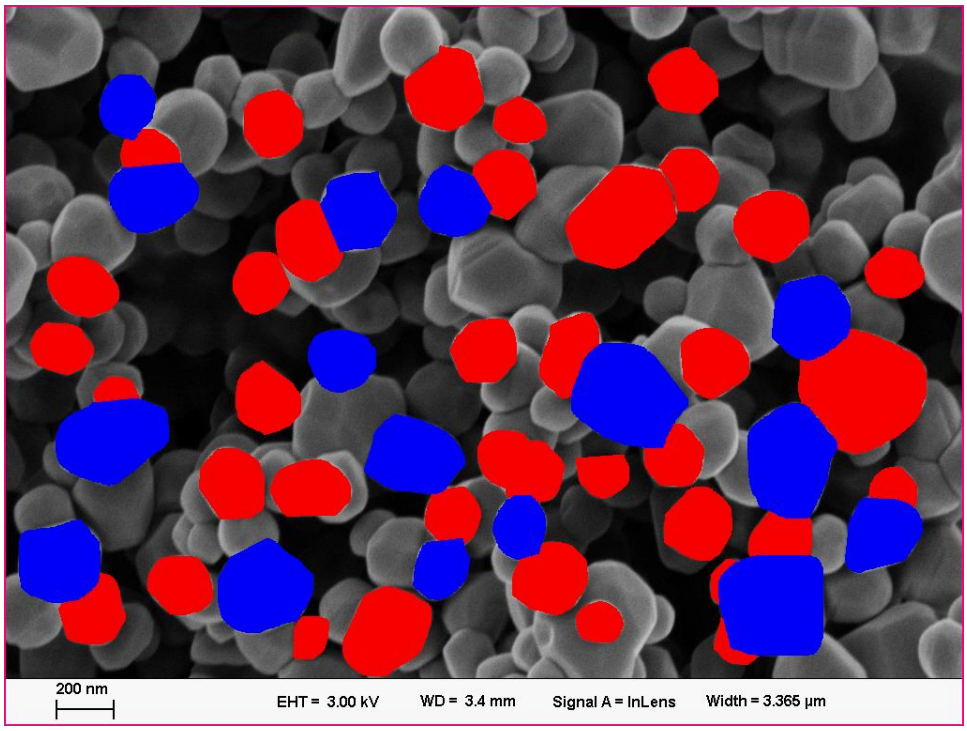

Figure 3: Image analysis performed on the 0.3 µm particles using the Clemex image analysis software. Red and blue were used to highlight/distinguish particles that share relatively flat boundaries. Over 500 particles were analyzed and the data was compiled to give a particle size distribution.

SEM images showed highly faceted Sumitomo AA-03, 0.3 µm and AA-3, 3 µm Al_2O_3 particles (Figure 4A and B). The 0.3 µm particles agglomerated together whereas the 3 µm particles were well dispersed. SEM image analysis showed that size distribution of the AA-03 peaked at 0.23 µm, which was slightly less than the 0.3 µm expected size (Figure 5).

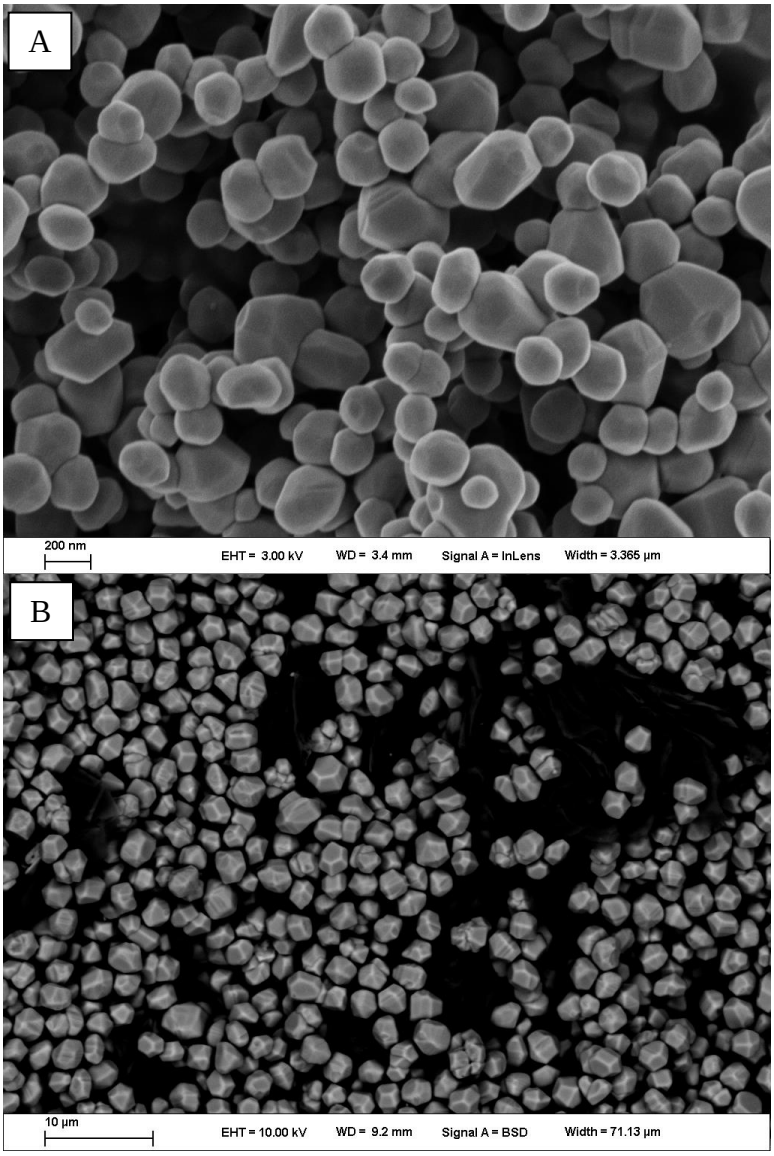

Figure 4: SEM images of A) 0.3 µm and B) 3 µm Al_2O_3 particles. Both particle sets appeared to be single crystalline and faceted.

2.1.2 Aerosol Generator and Particle Counter

A fluidized bed aerosol generator (3400A, TSI Inc., Shoreview, MN, USA) was used to disperse the particles. In this aerosol generator, bronze beads were used to break up the powder agglomerates. A scanning mobility particle sizer (SMPS, TSI Inc., Shoreview, MN, USA) and aerodynamic particle sizer (APS, TSI Inc., Shoreview, MN, USA) were used to measure aerosol concentrations and particle size distributions of sub-micrometer and supramicrometer particles, respectively [19].

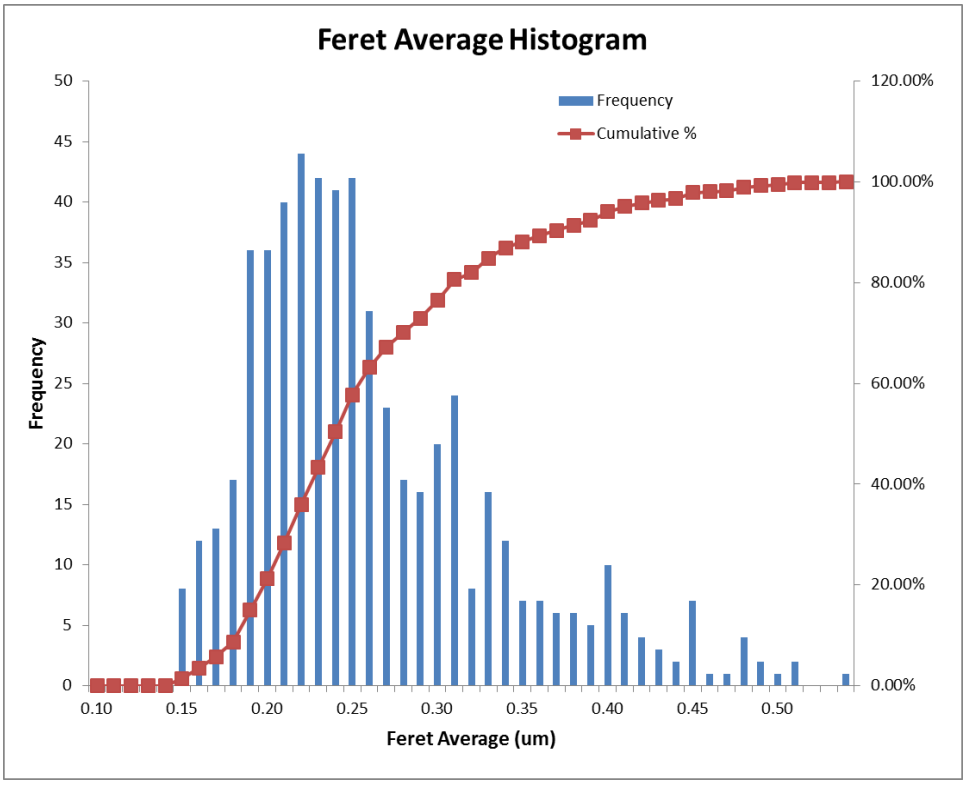

Figure 5: Particle size (ferret diameter) distribution of the Sumitomo AA-03, 0.3 µm Al_2O_3 particles measured using the Clemex image analysis software. Particle size peaked at ~0.23 µm.

On the other hand, the particle size measured in particle stream from the aerosol generator showed several peaks in the distribution (Figure 6). This is because the as-received 0.3 µm Al_2O_3 particles were agglomerated together and fed into the aerosol generator. In the aerosol generator, only some of the Al_2O_3 agglomerates were broken up by the bronze beads into individual 0.3 µm Al_2O_3 particles. Thus the particle stream from the aerosol generator consisted of three populations, the large Al_2O_3 agglomerates (green curve in Figure 6, peaked at 1 µm), the individual Al_2O_3 particles (broken up by bronze beads, red curve in Figure 6, peaked at 0.23 µm), and the bronze bead residue (blue curve in Figure 6). The AA-3 particle distribution peaked at 3 µm as expected (Figure 7).

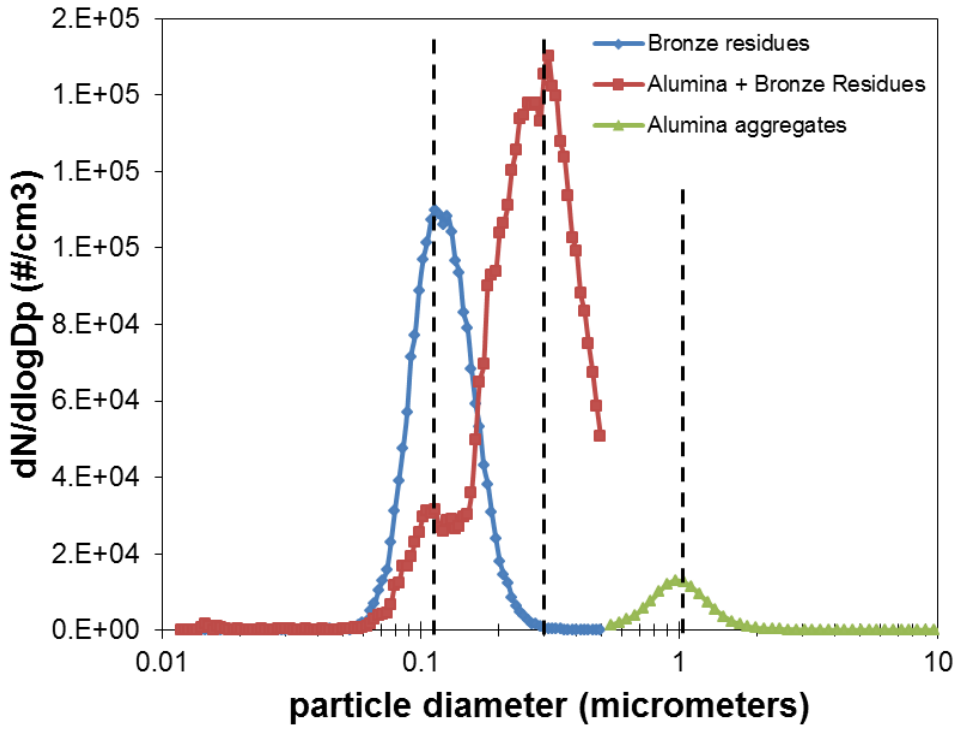

Figure 6: Particle size distribution of the Sumitomo AA-03, 0.3 µm Al_2O_3 particles measured using the aerosol generator (with bronze beads that break up agglomerates) and particle counter. Well dispersed particle size peaked at ~0.3 µm. Agglomerated particle size peaked at ~1µm.

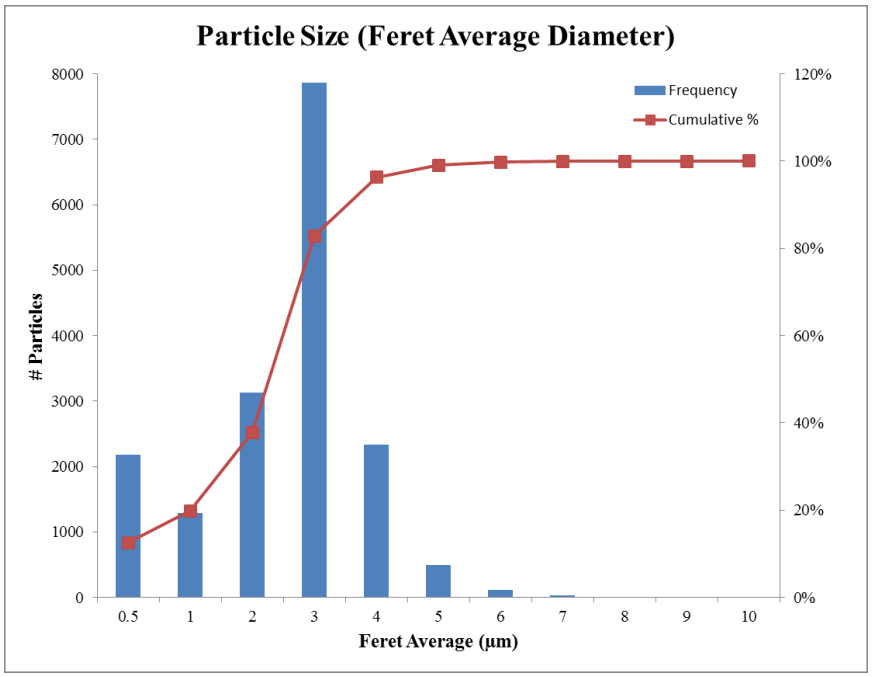

Figure 7: Particle size distribution of the Sumitomo AA-3, 3 µm Al_2O_3 particles measured and analyzed using the automated Oxford Inca Feature analysis suite.

2.2 Phase, Crystallinity, and Chemical Composition

2.2.1 X-ray Diffraction

X-ray diffraction (XRD) patterns were collected from the 0.3 µm and 3 µm Al_2O_3 powders to identify crystal structure/phase. XRD was performed using a Siemens θ–θ D500 diffractometer equipped with a sealed-tube source (Cu $K_{\alpha,}$ λ=0.15406 nm), a diffracted beam graphite monochromator, and a scintillation detector. Al_2O_3 powder samples were mounted on quartz zero-background holders for analysis. The conditions for each scan were fixed incident and diffracted beam slits (1° aperture), 10-80° 2θ scan range, 0.04° 2θ step-size, and a dwell time of 19 s/step. The XRD patterns were analyzed using JADE 9.6.0 software (Materials Data, Inc., Livermore, CA) equipped with the Powder Diffraction File PDF 4+ 2013 database (International Centre for Diffraction Data, Newtown Square, PA).

A powder XRD pattern collected from 0.3 µm Al_2O_3 particles is compared to a star quality ICDD PDF card in Figure 8. All peaks in the powder pattern collected from 0.3 µm Al_2O_3 can be indexed to PDF #00-046-1212 which confirms that the particles were α-Al_2O_3. The XRD pattern collected from 3 µm Al_2O_3 particles is shown in Figure 9 and was also confirmed to be α-Al_2O_3. No other phases were detected.

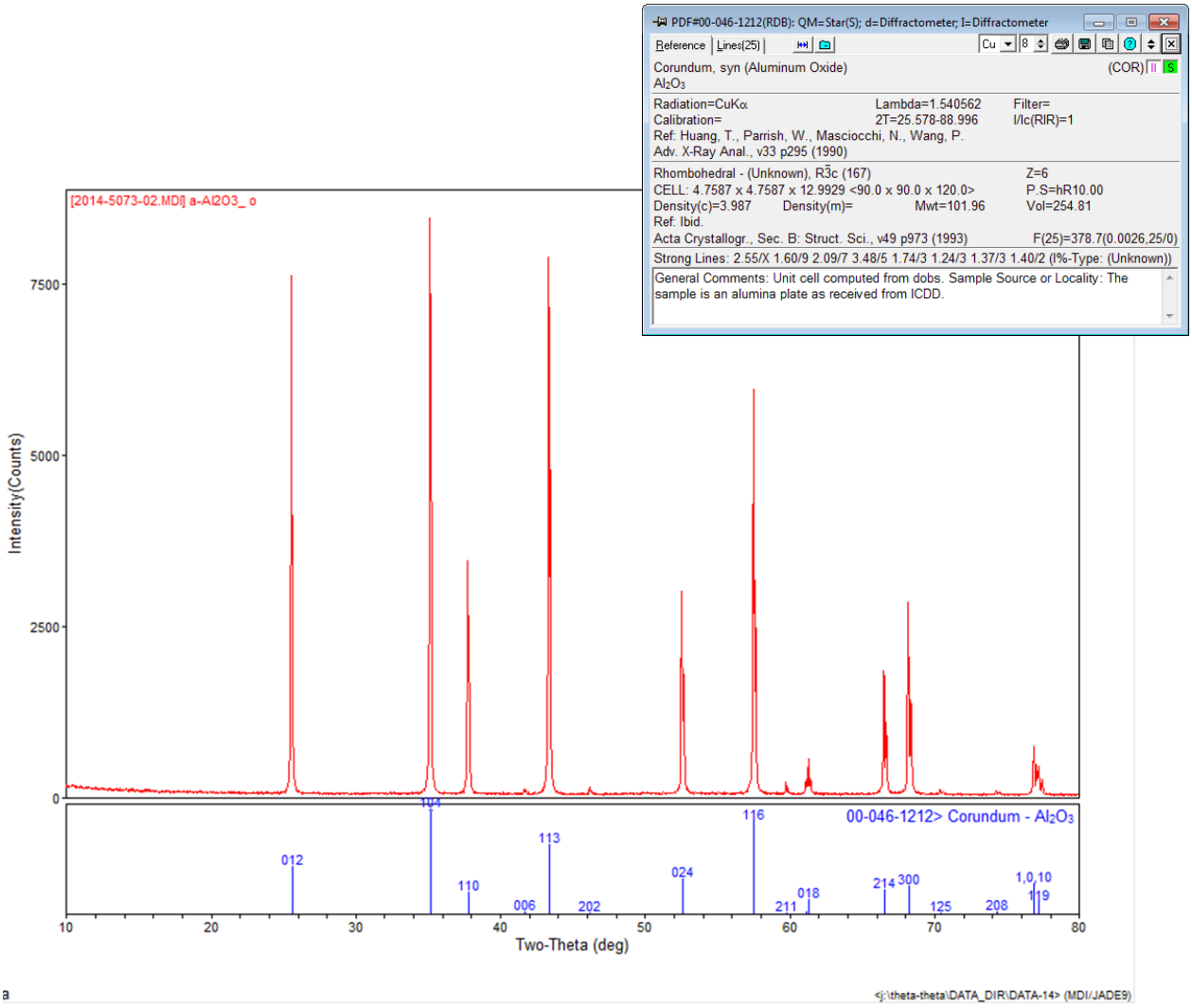

Figure 8: X-ray diffraction pattern collected from the 0.3 µm Al_2O_3 particles (red, above) and pattern showing relative intensity of corundum Al_2O_3 (blue, below). The patterns matched well, confirming the corundum structure of α-Al_2O_3.

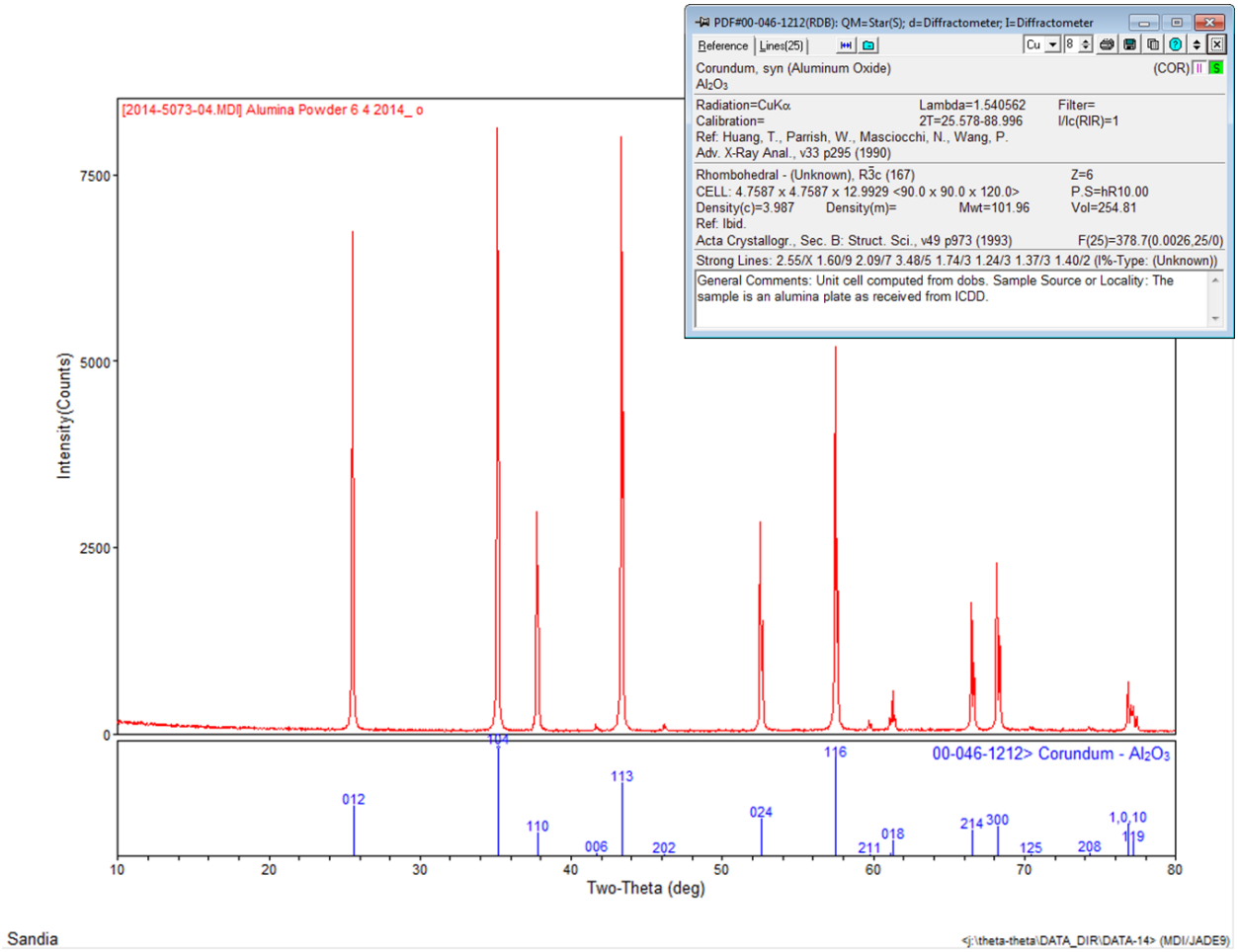

Figure 9: X-ray diffraction pattern collected from the 3 µm Al_2O_3 particles (red, above) and pattern showing relative intensity of corundum Al_2O_3 (blue, below). The patterns matched well, confirming the corundum structure of α-Al_2O_3.

2.2.2 Transmission Electron Microscopy (TEM)

The 0.3 µm alumina powder was dispersed in air onto a carbon-coated copper TEM grid. No further preparation was required as the particles were electron transparent.

The 3 µm particles were cross-sectioned using the focused ion beam (FIB) and prepared for subsequent TEM imaging. A FEI Helios dual platform focused ion beam (FIB) tool equipped with both a Ga+ ion column and a SEM column was used to produce cross sections of the particle samples for TEM imaging. Localized platinum deposition was used to protect the surface of the sample from direct ion beam irradiation. Thin samples for TEM analysis were produced by the *in situ* lift-out technique. A selected area of the sample was cut free using the ion beam. The cut sample was then transferred to a support Cu grid where final ion thinning was conducted.

Microscopy was performed with a FEI Tecnai F30-ST TEM/STEM operated at 300kV and equipped with an energy-dispersive x-ray spectrometer. A combination of TEM (bright and dark-field) and STEM (bright and dark-field) and selected area diffraction were used to determine

defects in the particles. X-ray spectra were taken from the particles to detect chemical elements (and possible impurities). The estimated sensitivity of EDS on this system is approximately 0.5 at% under the conditions used.

A combination of TEM (bright and dark-field) and STEM (bright and dark-field) and selected area diffraction were used to determine that the 0.3 µm particles were largely defect free, α-phase single-crystals (Figure 10). Moreover, the particles were found to agglomerate with some fraction having sintered to other particles, consistent with the SEM images in the previous section. Figure 11A shows an agglomerate of Al_2O_3 particles. Figure 11B and C show the two Al_2O_3 particles sharing a flat interface consistent with having sintered at high-temperature. The upper particle had several defects, likely dislocation loops, present (arrowed).

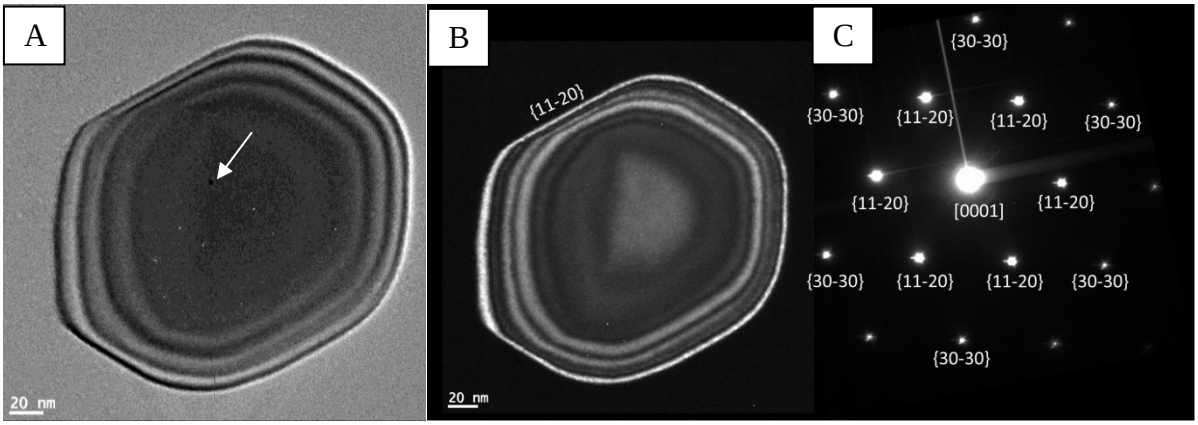

Figure 10: Bright field TEM image of A) a 0.3 µm Al_2O_3 particle, B) dark field TEM image of the same particle, and C) a diffraction pattern consistent with that of corundum. Facetted particle oriented on the [0001] zone axis. White arrow in A points to a dislocation loop.

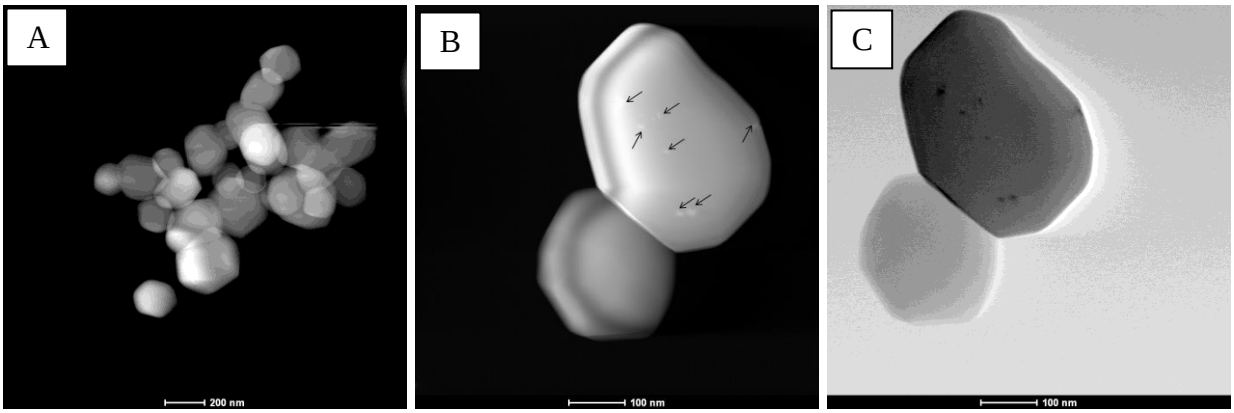

Figure 11: A) Dark field TEM images of 0.3 µm Al_2O_3 agglomerate and B) two alumina particles sintered together, and C) a bright field TEM image of two alumina particles sintered together. The spots within the particles in B and C were dislocation loops.

Figure 12 shows TEM images and diffraction patterns from several nominally three micron alumina particles. Figure 12A and B are bright-field and dark-field TEM images of a 3 µm particle that is free of dislocations but contains a low-angle grain boundary (lower part of grain). Figure 12C is a weak-beam dark field image of another 3 µm alumina particle with numerous defects. This grain is a single crystal albeit with several defects including dislocations and

stacking faults. Figure 12D is a selected area diffraction pattern showing reflections from one grain, confirming that the particle in Figure 12C, is a single crystal.

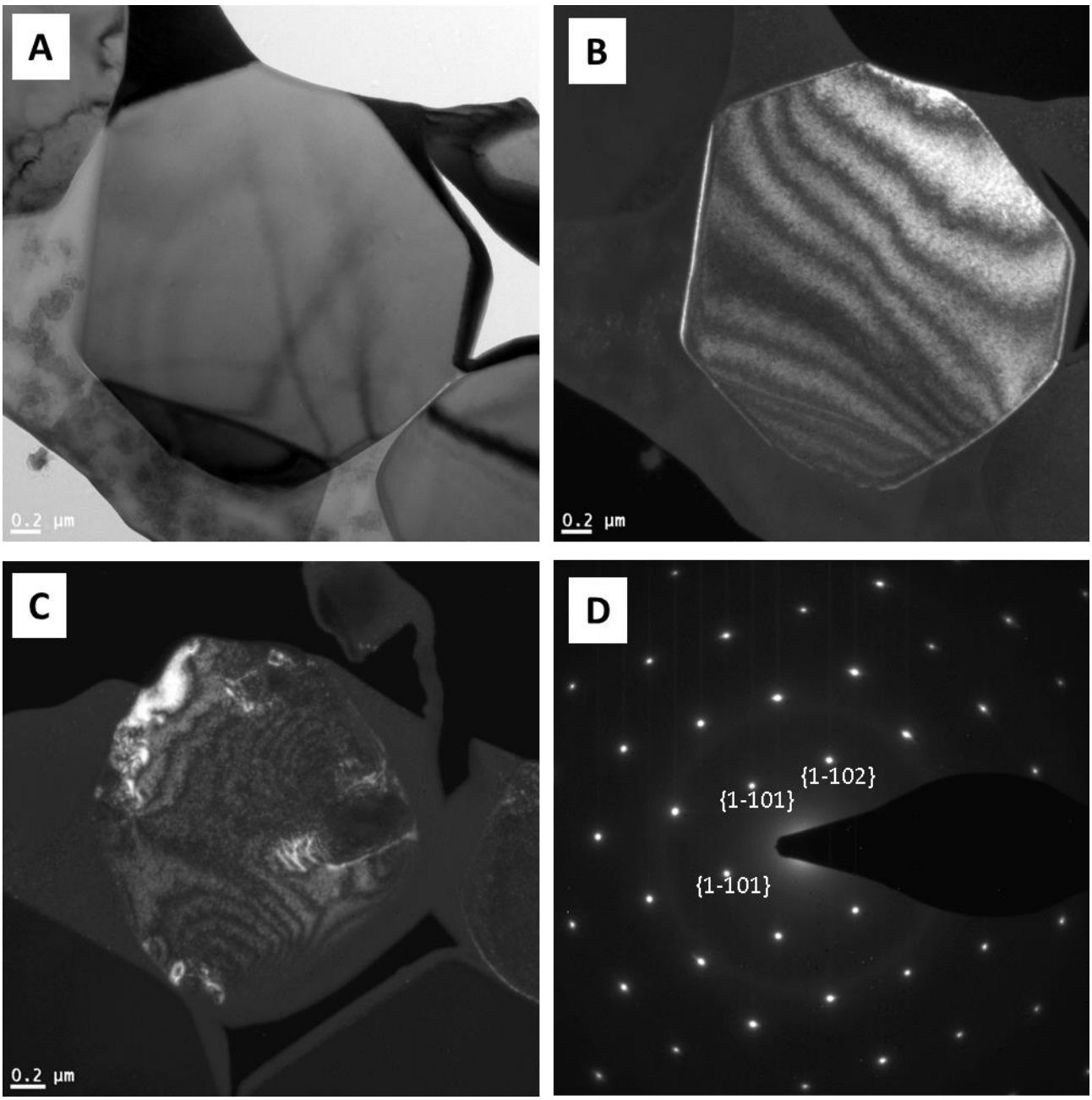

Figure 12: A) bright-field TEM image and B) dark-field from the same largely defect free single crystal particle. Note the dark region in the lower part of the particle in A is another grain; C) a weak-beam dark-field TEM image of different a single-crystal but defective particle; and D) the corresponding selected-area diffraction pattern (from particle in C) showing the single-crystal particle oriented on a zone axis.

X-ray spectra taken from the 0.3 µm particles showed that the material was clean with no other detectable elements but Al and O from the Al_2O_3 particles and Cu from the TEM grid (Figure 13). The estimated sensitivity of EDS on this system is approximately 0.5 at% under the conditions used. This suggested that the Sumitomo AA-03 particles are of high purity.

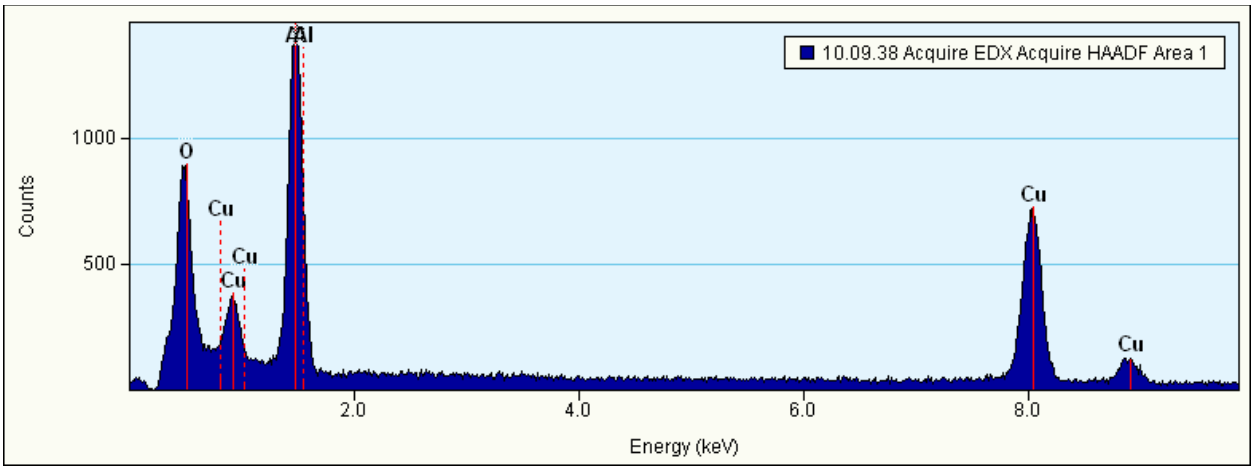

Figure 13: EDX spectra collected from the alumina particle agglomerate shown in the left of Figure 11. The only elements detected were Al and O from the Al_2O_3 particles and Cu from the TEM grid.

2.2.3 Inductively Coupled Plasma Analysis

The samples were dissolved in triplicate. Inductively Coupled Plasma (ICP) analysis was performed with a Perkin Elmer ICP-OES Optima 5300 DV. Samples were analyzed semi-quantitatively to identify trace metals present at levels above 5µg/g of Al_2O_3. Samples were then analyzed quantitatively for the identified metals.

The ICP analysis suggested very small traces of Sc and Zn as contaminants in the alumina powder. The results are shown in ug/g of original sample.

Element	Average	Standard Deviation
Sc	18.3µg/g	4.9µg/g
Zn	6.1µg/g	2.5µg/g

3. *IN SITU* COMPRESSION OF SUB-MICRON SIZED ALUMINA PARTICLES IN THE TRANSMISSION ELECTRON MICROSCOPE

An *in situ* ion irradiation transmission electron microscope (TEM) allows high spatial resolution and real time observation of the 0.3 μm electron transparent alumina particles under mechanical loading (nanoindentation). The 0.3 μm electron transparent alumina particles were suspended in ethanol, sonicated, and dispersed on single crystal sapphire substrates. As the alcohol evaporated, the alumina particles were left on the surface. *In situ* compression in the TEM was performed at SNL's I^3TEM facility [21] using a 200 kV accelerating voltage. The system (Figure 14) consists of a 200 kV JEOL 2100(HT) TEM with the LaB_6 filament, a 6 MV EN Tandem Van de Graaff – Pelletron accelerator, and a 10 kV Colutron G-1 ion accelerator.

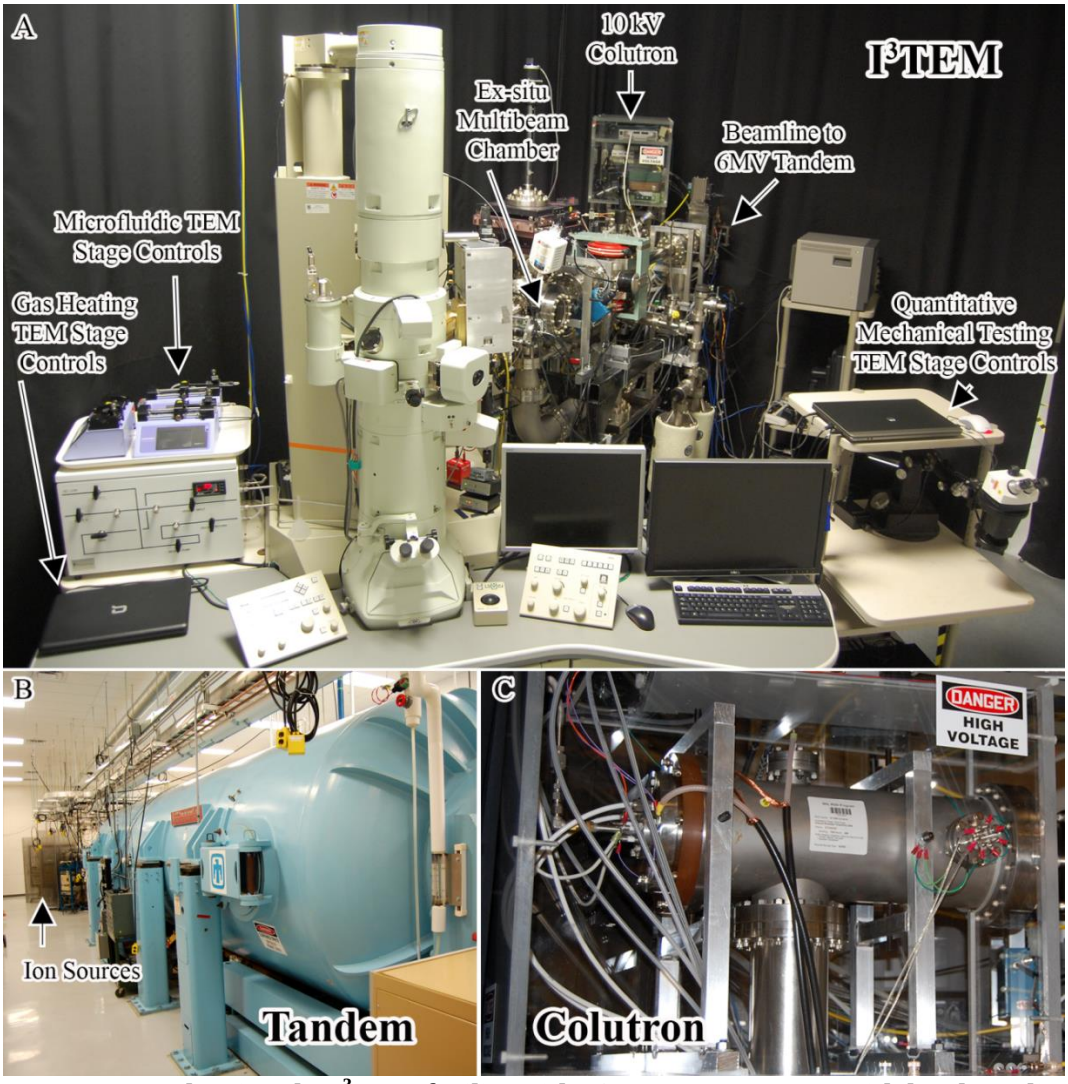

Figure 14: Images showing the I^3TEM facility with A) JEOL 2100 TEM with key beamline and stage capabilities identified; B) 6 MV EN Tandem Accelerator with the location of the ion sources identified; and C) The Colutron [20].

High tilt pole piece and the Tietze video and image processing systems (TVIPS) cameras were used. The 1024 x 1024 camera was used for recording videos at 15 frames per second (FPS). The 4048 x 4048 camera was used to record still images. The Hysitron PI95 indenter with a 1 μm diameter flat punch indenter tip was used. The indenter transducer has a maximum force of approximately 3 mN. Videos were recorded at 100k magnification during compression. The compression parameters for three particles are shown in Table 1.

Table 1: *In situ* compression parameters for particles in the TEM

Compression Parameters with Open Loop	Particle A, indent I	Particle A, indent II	Particle 3	Particle 4
Final Force (μm)	200	500	600	600
Seg. Time (s)	40	50	60	60
Loading Rate (μN/s)	5	10	10	10
Data Acquisition Rate (Points/sec)	200	200	200	200

The electron transparent, sub-micron sized 0.3 μm diameter particles exhibited ductile deformation in compression. During compression, the sub-micron sized particles showed dislocation activities, significant plastic deformation and fracturing. Figure 15 and Figure 16 show a 0.3 μm diameter particle ("particle 1") before and after compression.

After compression, dislocations were found in the particle. Dark field images showed multiple high dislocation density regions in the particle (Figure 16A-C). Corresponding diffraction patterns from different areas of the particle appeared to be tilted varying amounts about a single zone axis, indicating that the particle became polycrystalline (Figure 16D-F).

A detailed examination for compression of particle 2 will be discussed. Images of particle 2 before and after compression are shown in Figure 17. Load vs. displacement curves for two compressions of particle 2 (open loop mode at 10 μN/s loading rate) are shown in Figure 18. During the first compression (black curve in Figure 18), a surface asperity caused particle 2 to roll initially. Eventually the particle reached a position where it stopped rolling. The subsequent compression remained purely elastic, and no defect production was observed within the particle. During unloading, the particle rolled back somewhat, but not entirely to its original position. In the second compression, the particle only rolled slightly before undergoing elastic deformation, then plastically deforming starting at 307μN. This transition from elastic to plastic deformation can be seen through the change in slope of the load vs. displacement curve (red) in Figure 18. The displacement excursion (burst) from 77 nm to 84 nm corresponding to a fracture event occurred at a load of 433 μN. The tip was able to keep up with the displacement excursion and the loading continued to 446 μN before the tip was retracted. It is important to note that the particle fractured but did not separate into pieces (Figure 18B). TEM dark field images of the particle are shown in Figure 19. The dark field images showed high dislocation density regions in the particle in different diffracting conditions. Diffraction patterns collected at the left (Figure 20A), middle (Figure 20B), and right (Figure 20C) of the particle showed that the two halves of the particle were rotated into different orientations, confirming that the particle had fractured.

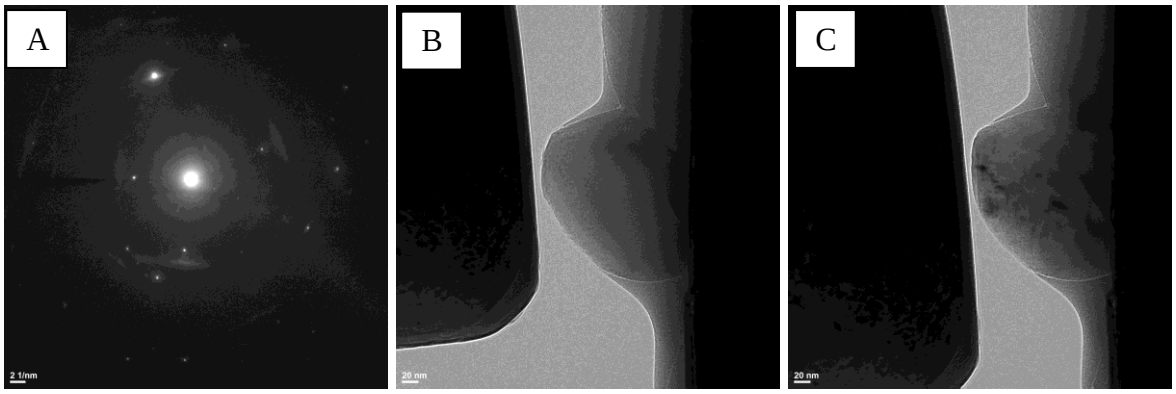

Figure 15: A) Diffraction pattern of the 0.3 µm particle 1 before compression, B) Bright field TEM images showed particle was relatively defect-free before compression, and C) was full of defects after compression. The compression was performed in open loop control mode.

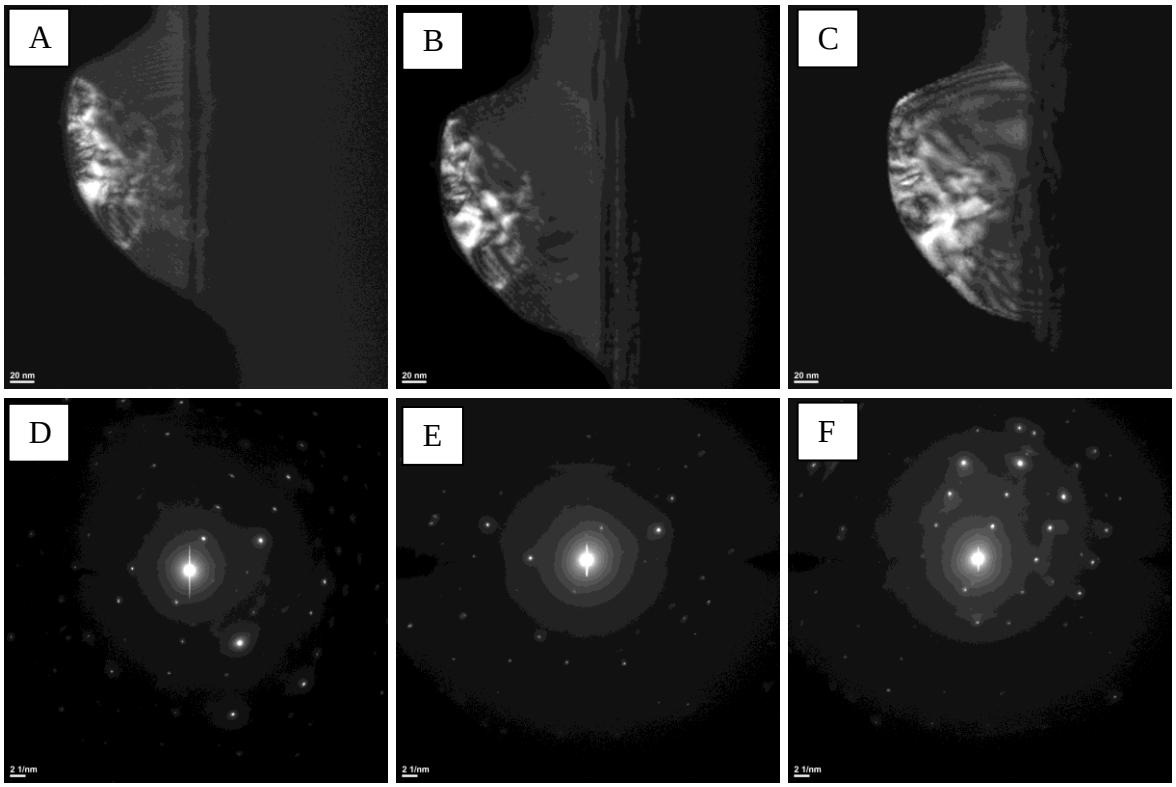

Figure 16: Dark field TEM images of the AA-03 (0.3 µm) particle 1 after compression (A,B,C) showing high dislocation density in different diffracting conditions and corresponding diffraction patterns from different areas of the particle (D,E,F) suggesting polycrystallinity after compression.

In addition to the observed apparent deformation/fracturing behaviors, two quantitative measures of ductility are the accumulated strain that the particle can withstand in compression before fracturing and the critical energy release rate, G_C. *Gc* values were demonstrated in literature for Si particles fracturing in compression [21]. In this work, approximated accumulated strain was taken to be the total displacement divided by the initial particle diameter and the approximated G_C can be extracted from the load vs. displacement data.

Strain energy release rate value is closely related to the fracture toughness through (eq. 1) with a lower value of G_C indicating lower ductility:

$$G_C = K_{IC}^2/E \quad \text{(eq. 1)}$$

where K_{IC} is the critical stress intensity factor and E is Young's modulus. For bulk alumina, K_{IC} = 44 MPa$\sqrt{m}$ and E = 375 GPa [22], which gives a value of G_C = 40 J/m^2.

The G_C of most brittle ceramics is ~10s J/m^2 where as that of ductile metals is ~1,000s J/m^2. The approximated G_C values of the compressed particles suggested the nature of deformation behavior (i.e. whether the deformation is similar to brittle ceramics or ductile metals). The first order of approximation for strain energy release rate during compression of the 0.3 μm particles can be calculated from the collected load vs. displacement curves. In this work, the G_C was estimated from the energy (area under the displacement *burst* obtained from *in situ* compression in the TEM) divided by the fracture surface area (two times the cross-sectional area of the particle before compression).

The fracture (or deformation) energy release rate, G_C, can be estimated by integrating the area under the displacement burst (area under the red curve, highlighted in red in Figure 18) for particle 2. With fracture, the energy can be normalized by the new surface area created. In order to estimate the G_C, it was assumed that fracture went through the center of particle. The first order of estimation was: energy of 7 nm * 435 μN = 305 pJ and particle diameter of 370 nm, providing the G_C of 1386 J/m^2. This particle fracture energy is much higher (i.e. the particle is more ductile) than G_C for bulk Al_2O_3 (40 J/m^2) and other ceramics.

It is important to note that the electron beam deposits some energy within any material it passes through, and hence may have some effect on the plasticity of the particles here. Significant global heating is not expected, but enhanced local diffusion may result from particularly strong electron interactions within the sample [23]. Further work is needed to quantify the extent of any electron beam effects during these or similar tests. However, the relatively low electron dose rate (<50 pA/cm^2), short duration of the compression tests (30 – 60 s), and crystalline structure of the particles all contribute to a diminishing influence of the electron beam.

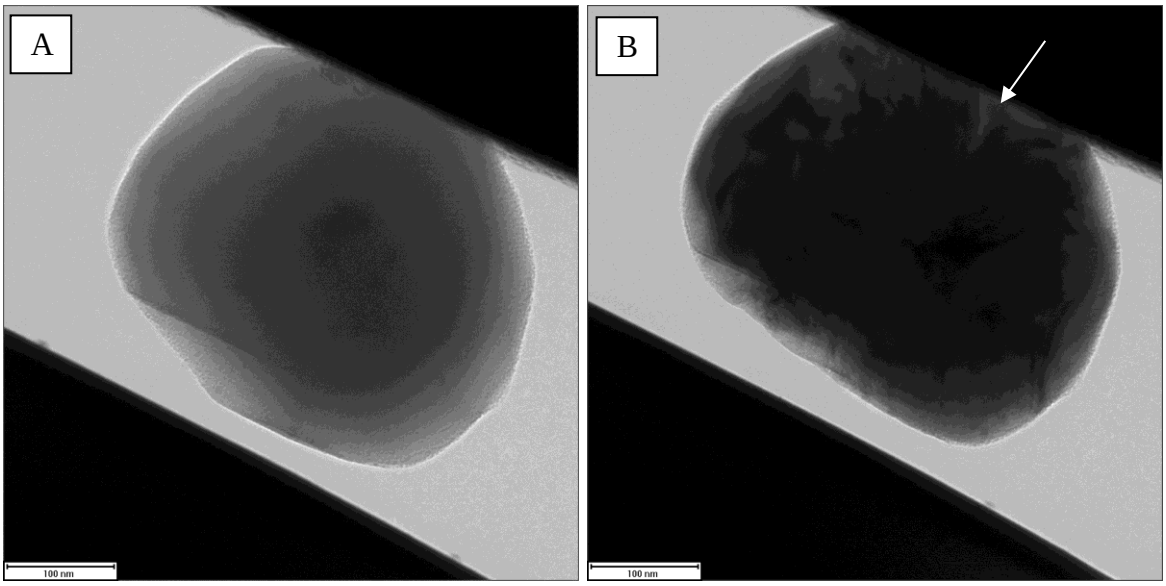

Figure 17: TEM bright field images of particle A, A) before and B) after compression. The arrow indicates fracture line.

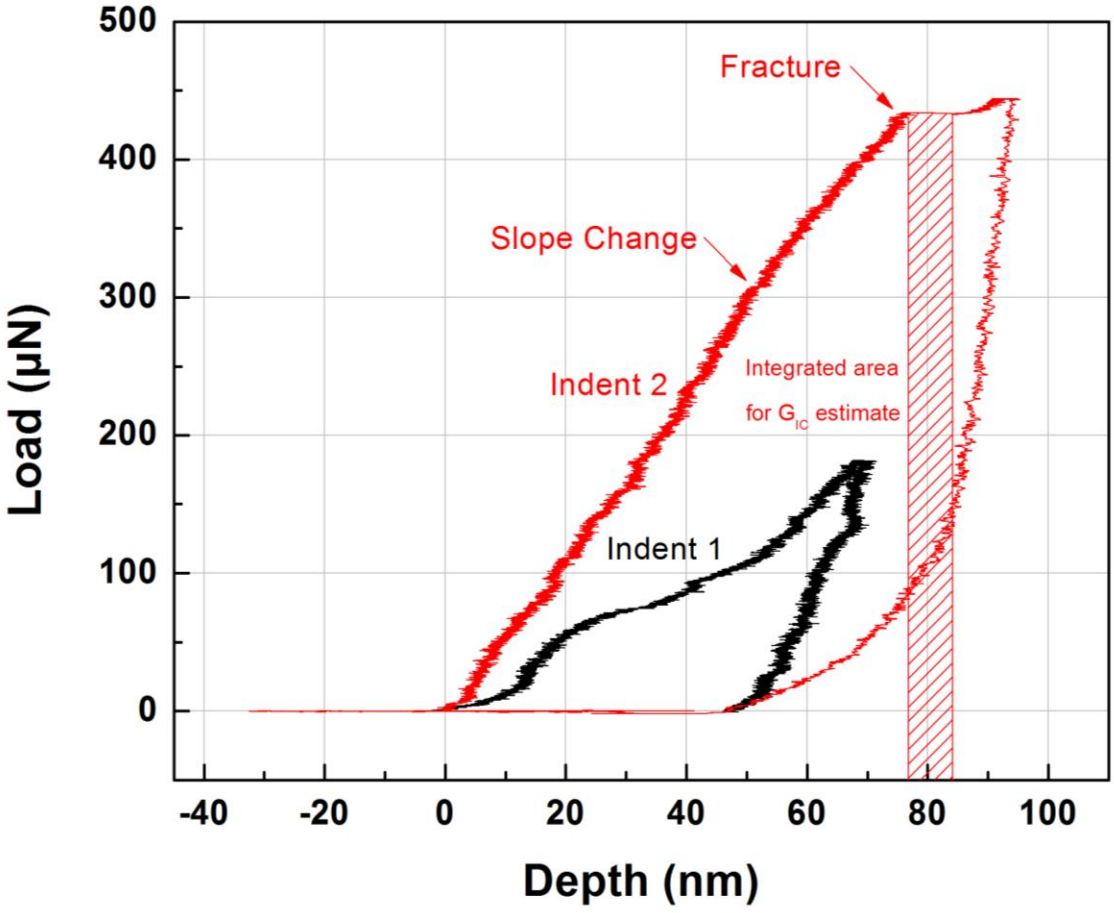

Figure 18: Forces as a function of displacement collected during two open-loop nanoindentations on a single, 0.3μm, Al_2O_3 particle "A". Indent 1 (red curve), particle was loaded elastically and rolled with peak load of 180 μN. Indent 2 (blue curve), particle was loaded elastically and plastically before fracturing at the peak load of 435 μN.

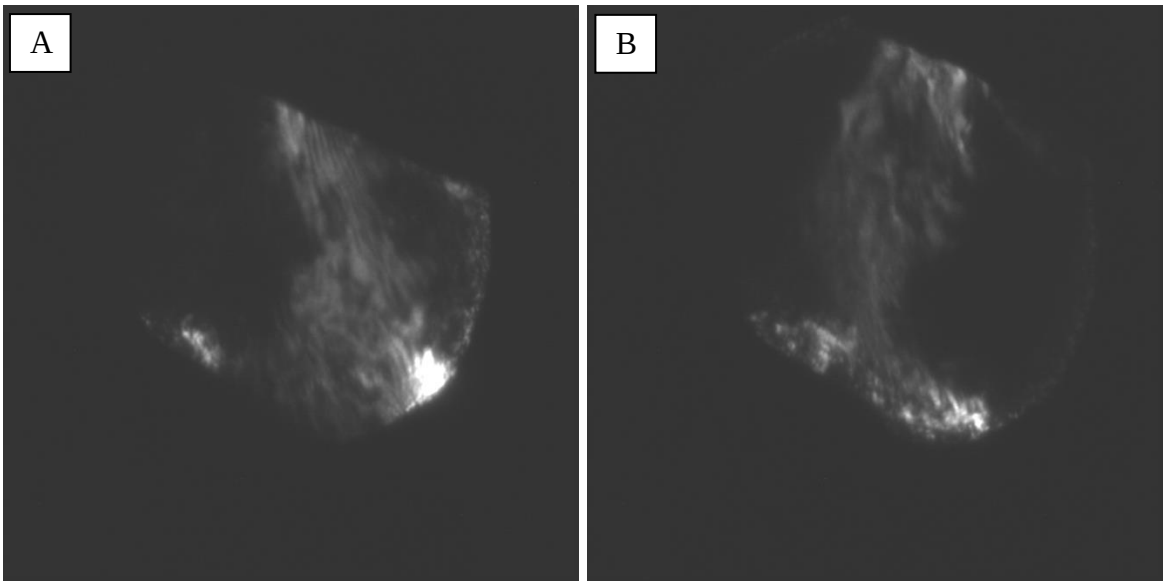

Figure 19: TEM dark field images of particle A after compression in different diffracting conditions. Both A) and B) showed areas with high dislocation density (appearing light in the images) within the particle.

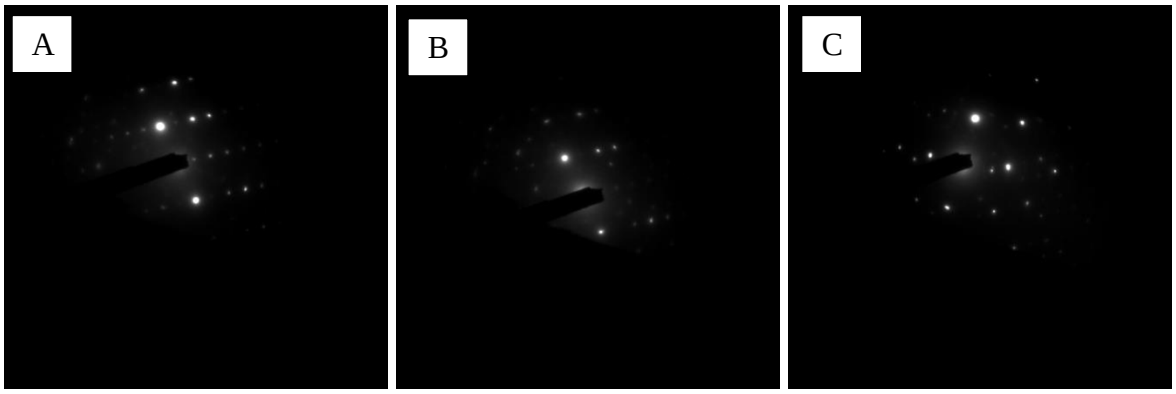

Figure 20: Diffraction patterns collected on particle A after compression at A) left side of the particle, B) middle of the particle, and C) right side of the particle. These diffraction patterns confirmed that the particle fractured and the two halves have different orientations.

4. *IN SITU* COMPRESSION OF SUB-MICRON AND MICRON SIZED ALUMINA PARTICLES IN THE SCANNING ELECTRON MICROSCOPE

The effect of particle size on deformation behaviors in Al_2O_3 was investigated by loading particles with nominal diameters of 0.3 μm and 3 μm in compression *in situ* with a nanoindenter inside an SEM. Particles were deposited on a sapphire substrate by suspending them in methanol or ethanol, sonicating the mixture, and then placing a drop of the mixture onto the single crystal sapphire surface. As the alcohol evaporated, the Al_2O_3 particles were left on the surface. Surfaces were sputtered with a thin layer of gold (on the order of nm) for 15 seconds to alleviate charging in the SEM from the particles and the single crystal sapphire substrates.

Before loading, a sample of particles was imaged in plan-view (0°) in the SEM to select particles for loading, for measuring particle geometry/size from this angle, and for comparison to later plan-view images of the deformed particles. Loading was performed at an angle of 86° so that the indentation process could be observed *in situ*. Loading was performed using an *in situ* Hysitron PI85 SEM Picoindenter (Figure 21) with a 3 μm diameter tip for 0.3 μm particles and a 6 μm diameter tip for 3 μm particles.

During loading, video comprised of successive SEM images, was recorded concurrently with load vs. displacement data. Specimens were loaded in a "displacement control" mode. Micron sized particles with a diameter of 3 μm were loaded at a displacement rate of 8 nm/s while sub-micron particles with a diameter of 0.3 μm were loaded at a displacement rate of 15 nm/s. Normalizing these displacement rates by the particle diameter gives nominal strain rates of 0.003 and 0.05 s^{-1}, respectively (strain is defined here as displacement divided by the particle height). Images of particles before and after deformation were captured at several angles for comparative analysis.

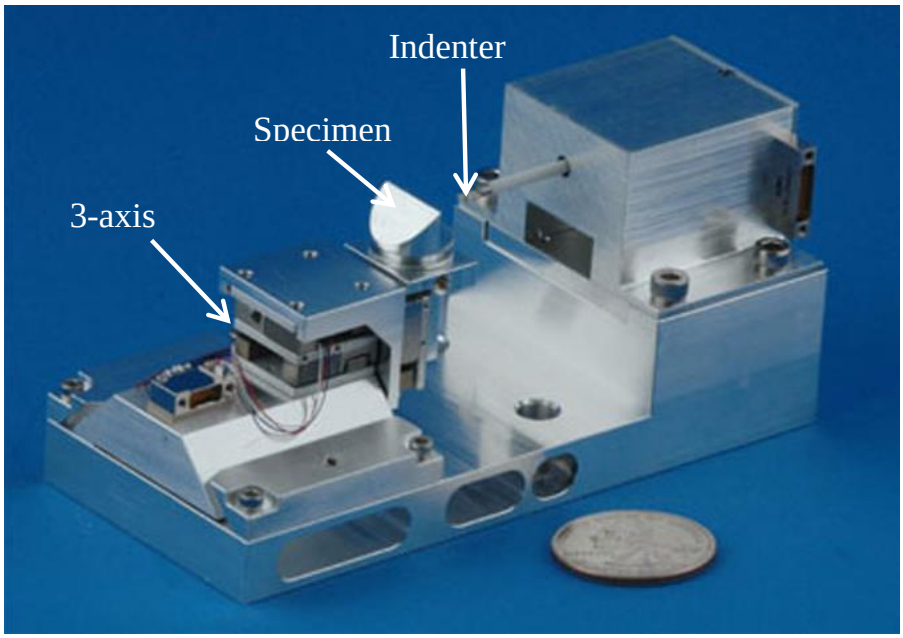

Figure 21: PI 85 SEM Picoindenter, Hysitron, Inc. [24]

The sub-micron sized Al_2O_3 particles also deformed in a ductile manner in the in situ SEM compression experiments. After compression, the sub-micron sized particles showed significant plastic deformation and fracturing as shown in Figure 22. Each compressed sub-micron sized particle stayed intact as a single entity even with fractures. The compression of particle 3 and particle 4 in Figure 22 were stopped after observing a drop in force vs. displacement curves. After releasing, significant deformation and cracking were observed in the particles. On the other hand, particle 1 was loaded to the extreme. After releasing, particle 1 appeared 'flattened', showing significant deformation and cracks. It was noteworthy to observe the similarity of this compressed and 'flattened' 0.3 μm Al_2O_3 particle 1 in this experiment to the reported compressed 0.5 μm Al_2O_3 particle previously displayed in Figure 1 [1]. This confirmed that sub-micron sized alumina particles can undergo significant plastic deformation and cracking simultaneously without cleaving apart into pieces.

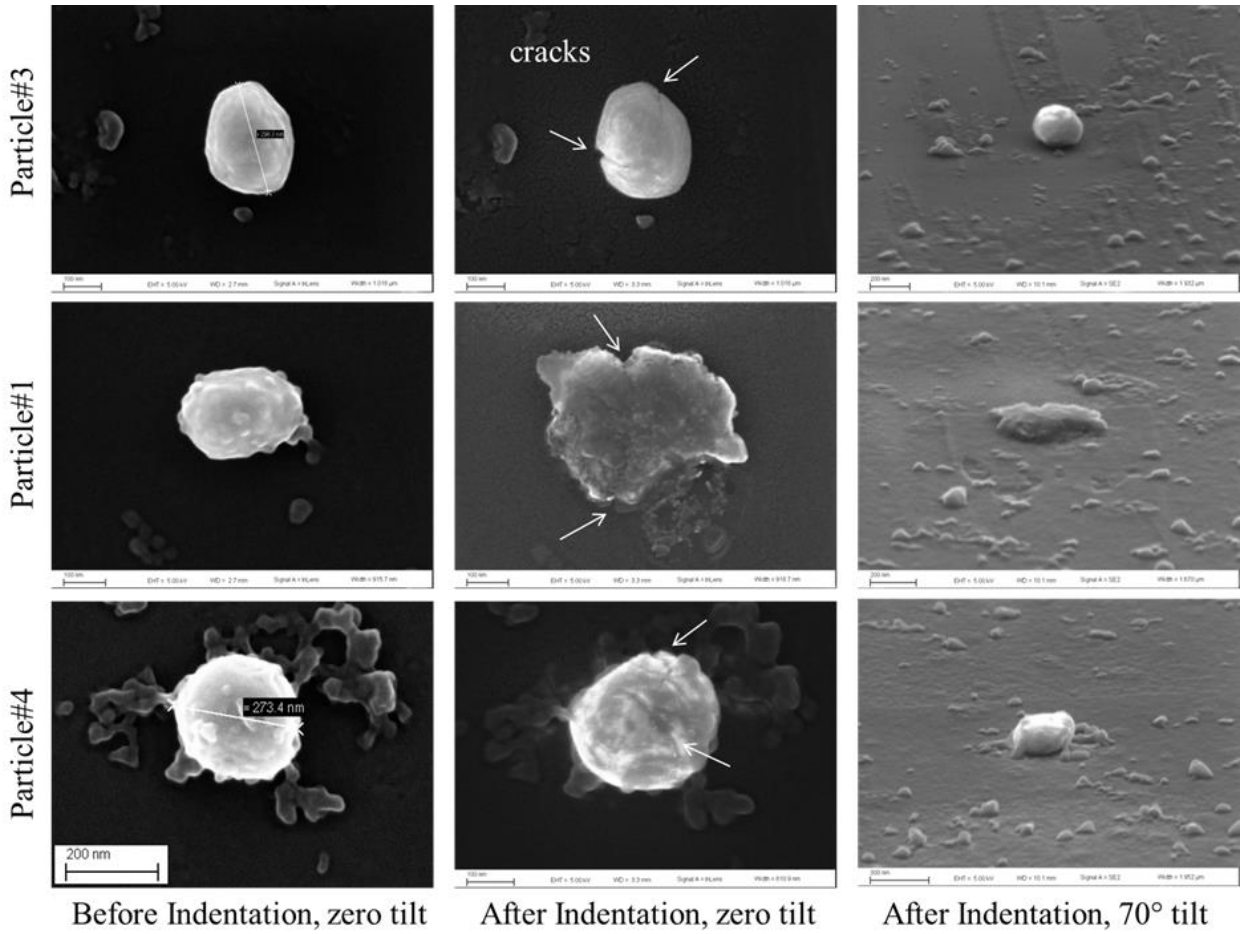

Figure 22: Top view SEM images of three AA-03 (0.3 μm) particles before (left column) and after (middle column) compression as well as tilted view SEM images of three particles after compression (right column). This figure showed different variations in deformation behaviors (plastic deformation, change in shape, cracks, etc.).

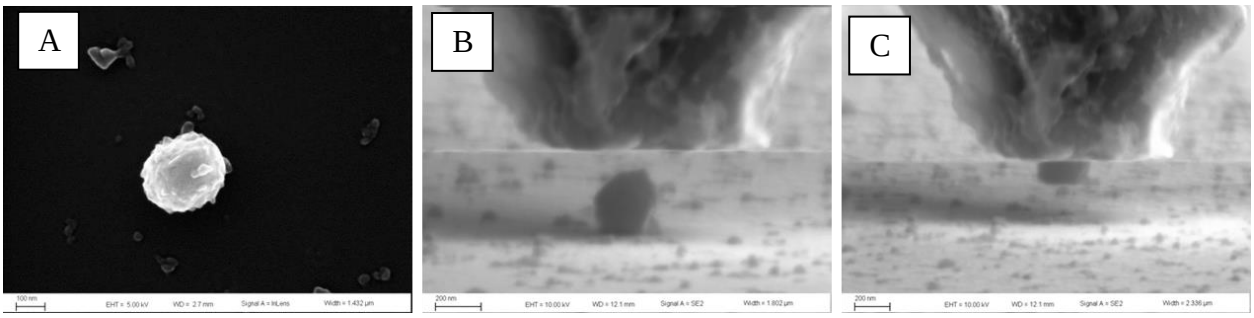

Figure 23: A) Top view SEM image of "particle 5" with 0.3 µm diameter and side view SEM images B) before compression and C) after compression. The particle was stuck to the tip after compression.

The load VS displacement curves and time-based plots of force and displacement for compression of particle 5 are shown in Figure 23. Although these tests were performed in displacement control mode, the control system was unable to keep up with the fast fracture event resulting in the displacement spike around 5.8 seconds (Figure 23B). The result of this was an apparent jump in displacement with an abrupt drop in load at the point of fracture.

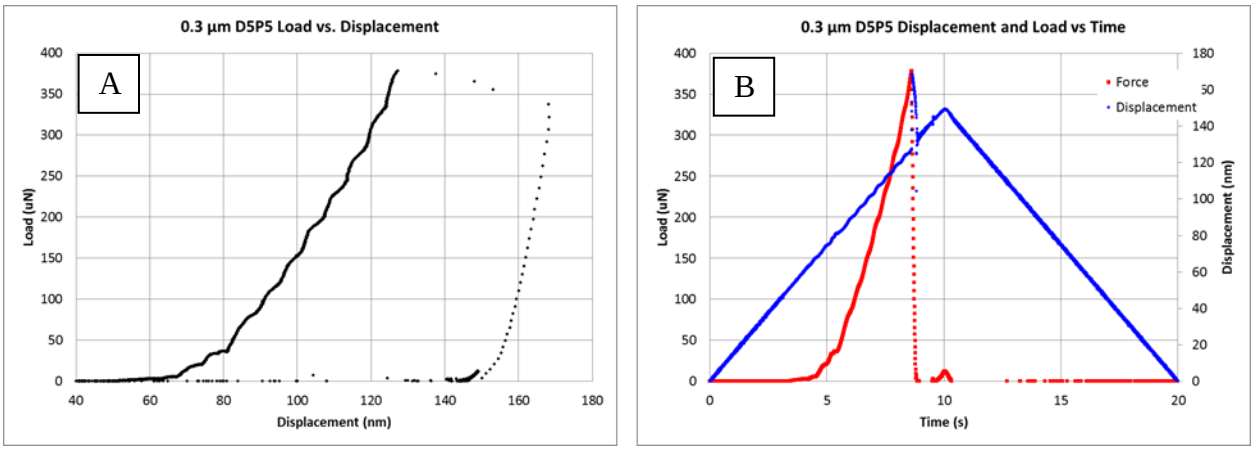

Figure 24: An example of loading data for a large particle, "particle #5", shown in Figure 23. A) Force VS displacement and B) force and displacement VS time. The control system was unable to keep up with the fast fracture event resulting in the displacement spike around 8 seconds (in B).

In contrast, the 3 µm diameter particles deformed in a brittle manner. Fast fracture was clearly observed through in situ SEM, and particles were left in several pieces after the fracture event such as those shown in Figure 25. No significant plastic deformation was observed. Load VS displacement curves and time-based plots of force and displacement for particle 5 are shown in Figure 26. The fast fracture event (and the resulting displacement jump) occurred around 51 seconds (Figure 26B).

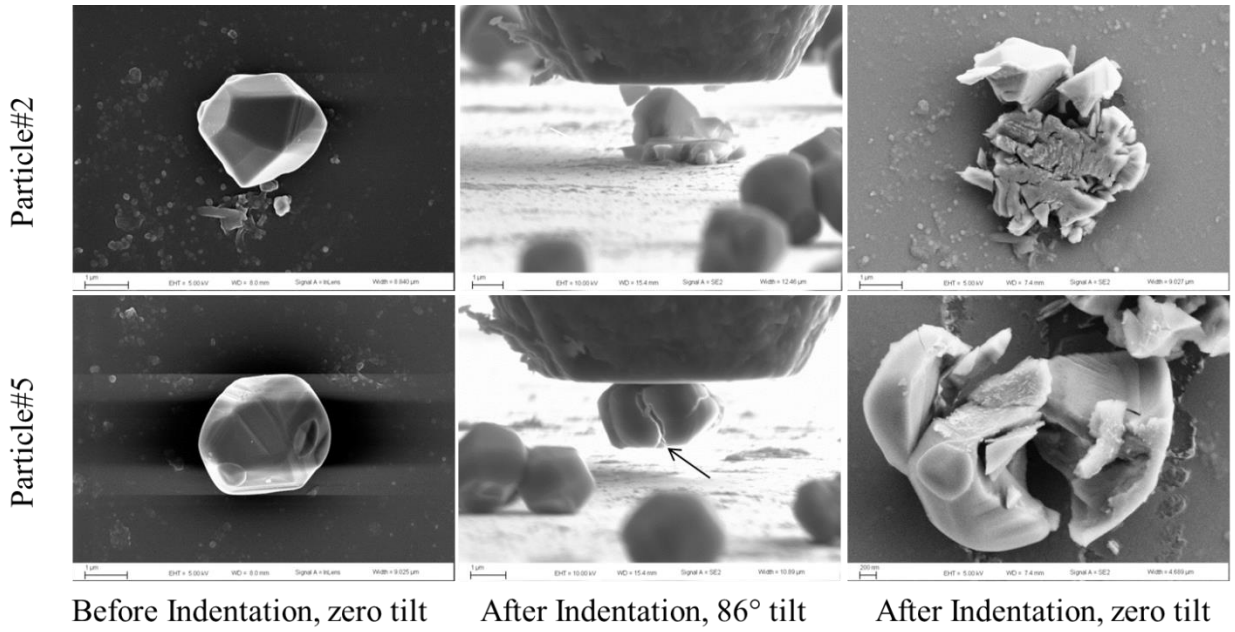

Figure 25: Top view SEM images of two AA-3 (3 µm) particles before (left column) and after compression (middle and right columns). Large particles fractured into pieces.

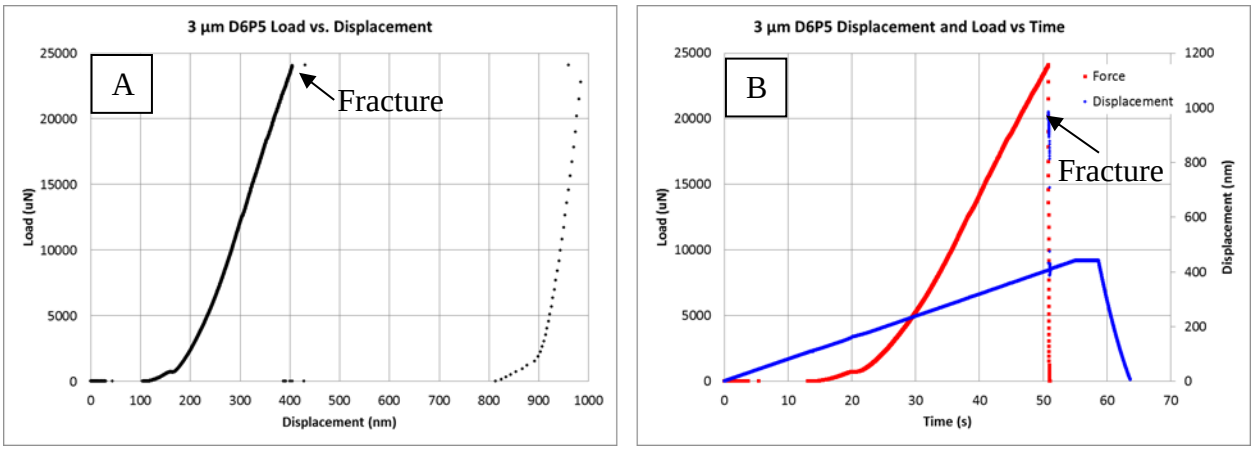

Figure 26: An example of loading data for a large particle, "particle #5", shown in Figure 25. A) Force VS displacement and B) force and displacement VS time. The control system was unable to keep up with the fast fracture event resulting in the displacement spike around 51 seconds (in B).

The failure modes observed in the SEM images and videos provide great insight to determine the deformation behaviors of the sub-micron and micron sized Al_2O_3 particles. As shown in Figure 25, large particles burst into several pieces upon fracturing. In contrast, small particles such as those shown in Figure 22 and Figure 23, often sustained cracking (e.g. particles 3 and 4), but remained together and exhibited substantial deformation (e.g. particles 4 and 1).

A more quantitative approach would be to consider the G_C. However, the G_C could not be accurately estimated from the load vs. displacement curves from the *in situ* compression of the 0.3 µm or the 3 µm particles in the SEM. The reason for this was because the system had difficulty maintaining a constant displacement rate when it experienced the sharp load drop

associated with sudden fracture, although these experiments were performed in displacement control mode. Consequently, a large displacement excursion occurred upon the onset of fracture (at 51 seconds in Figure 26). Integrating the area under this displacement excursion was not valid because the system did not keep up with the abrupt change in particle compliance due to fracture. Future experiments using an open-loop control mode should address this issue.

Another quantitative approach was used to determine deformation behavior of the sub-micron and micron sized Al_2O_3 particles. Definition of ductility is also how the particles withstand substantial deformation, corresponding to high accumulated strain under an applied load. In this work, strain is taken to be the displacement divided by the particle diameter. By this definition, the small particles behave in a much more ductile manner. As shown in the last column of Table 2, the 0.3 μm particles withstood two to three times the amount of strain before fracture as compared to the 3 μm particles.

Table 2 Compressed particle sizes, compression strain rates and corresponding accumulated strain at first fracture.

Particle Identifier	Diameter (μm)	Strain Rate (s^{-1})	Strain at First Fracture (%)
Large Particles			
D6P1	2.9	0.03	5
D6P2	2.6	0.006	5
D6P4	2.9	0.005	5
D6P5	2.9	0.003	7
Small Particles			
D5P2	0.17	0.09	11
D5P3	0.29	0.05	12
D5P4	0.28	0.05	13
D5P5	0.29	0.05	16

5. MOLECULAR DYNAMICS SIMULATION OF NANOPARTICLES UNDER COMPRESSION

Molecular dynamics (MD) tracks the motion of individual atoms in a given system, making the identification of dislocations, slip planes, and particle fracture possible. In order to correctly identify such events during compression of the particles, it is necessary to use a MD force field (FF) that allows for the formation and breaking of bonds between atoms. The simplest MD FFs assign bonds between neighboring atoms at the beginning of a simulation, without allowing for the possibility of these bonds breaking, or new bonds forming. Such a FF would not be appropriate for the current project. Instead, an FF developed by Garofalini's group at Rutgers University [25] that has accurately predicted surface structures, defect concentrations, and composition of intergranular films in a variety of ceramics, was implemented. While fracture surfaces have been studied with this FF [26], the authors are unaware of any studies of dynamic fracture. Another FF [27] is currently being explored to determine if our simulation results are universal.

The applicability of MD simulations in the interpretation of experimental results is often hampered by a large mismatch in time and length scales. Because MD requires accurate representation of atomic vibrations, timesteps for the numerical integration are on the order of 1 fs. The timestep constrains the simulation times to approximately tens of ns and velocities to greater than ~0.01 m/s. While massively parallel computers allow for simulations to be spread over many processors, the balance between intra-processor computations and inter-processor communications is generally most favorable at about $10^3 - 10^4$ atoms per processor, which in turn limits simulations to 10^6-10^7 atoms at most.

For the Al_2O_3 nanoparticles in this study, the computational limits described above imply that the largest NP amenable to MD has a diameter of approximately 500 nm (ca. 3×10^6 atoms), which limits the simulations to the regime of plastic deformation. It is hypothesized that the reason 'smaller' particles (diameter < 1μm) deform plastically while 'larger' particles (diameter > 1 μm) fracture is due to the former being defect-free single crystals, while the latter have initial defects present. In an attempt to circumvent this size issue, a variety of small NPs (diameter 10 nm) that are either single crystal or have a variety of initial defects were created. If it is, in fact, the presence of defects that lead to fracture rather than the actual size of the NP, then these systems should allow the authors to study NP fracture in systems that are still computationally feasible.

Snapshots of thin slices through the initial configurations of the three NPs studied are shown in Figure 27. These include a single crystal NP (Figure 27A), a NP with a vertically oriented grain boundary (hereafter referred to as a 'Janus' NP in Figure 27B), and the same Janus NP with a rectangular notch opened along the grain boundary (Figure 27C). A Janus NP with a triangular notch was also simulated. However, it was found that the triangular type notch for 'initial crack' healed upon equilibration due to successive rebonding across the crack, starting from the apex and continuing to the surface of the NP. Whereas results from the compression of NPs with this triangular notch are given below, no snapshots will be shown.

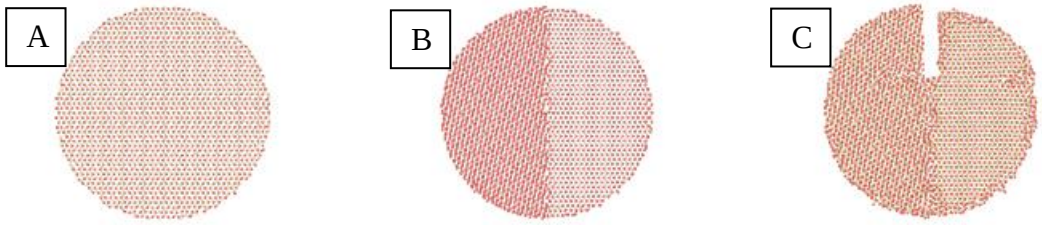

Figure 27: Snapshot of initial configuration of A) a single crystal nanoparticle, B) a Janus nanoparticle with a vertically oriented grain boundary, and C) a notched Janus nanoparticle showing location of initial crack.

The NPs were created from a bulk single crystal α-Al_2O_3 sample with the basal plane {0001} oriented vertically (i.e. perpendicular to the direction of compression). The single crystal NP was created by removing all atoms that did not lie within a prescribed distance from the center of the NP. This necessarily implied that a variety of crystal faces were exposed on the surface of the NP. To create the Janus particle, the single crystal NP was duplicated and given random rotations along the three Euler angles. The initial and rotated particles were cut in half along the z-axis and joined. Notches were created by moving all atoms along the upper third of the NP away from the grain boundary. Atoms were translated by distances linearly decreasing from 5 Å (for those initially at the grain boundary) to 0 Å (for surface atoms). The NPs were energy minimized at 0 K, followed by equilibration at room temperature for 1 ns.

To compress the particles, purely repulsive Lennard-Jones walls were created at a distance of 3 Å from the top and bottom of the NPs. These walls were moved together at a constant velocity of 200 m/s. Particles were compressed for an overall distance of 34 Å (approximately 1/3 the diameter of the particles) and then the direction of the walls was reversed. A plot of the overall calculated pressure of the system as a function of compression distance was created for each NP type.

MD simulations were performed on the Al_2O_3 NPs (10 nm diameter) in compression. The overall calculated pressure of the system as a function of compression distance for all NP types is shown in Figure 28. The zero of compression has been set to coincide with the first contact of the walls and the particles. During the first 8-10 Å of compression, there is essentially no difference in the pressure for the single crystal NP and the Janus NP, indicating that the grain boundary has little effect. The triangularly notched Janus NP is also nearly identical, indicating that the healing of the notch seen under equilibration results in a NP that is equivalent to the unnotched NP. The NP with the rectangular notch, shown in green in Figure 28, shows substantially smaller maximum pressure, although this could be due to the void space in the particle. It is particularly interesting to note that none of the curves in Figure 28 show pressure drops like those in literature [12] that have been ascribed to fracture events.

After compression, the walls are reversed to allow the particles to decompress, and indicate the extent of plastic deformation. While the pressure curves do indicate a negative pressure after approximately 2 Å of decompression, this is likely due to the elastic recovery of the particles, and should not necessarily be correlated with the negative forces measured experimentally.

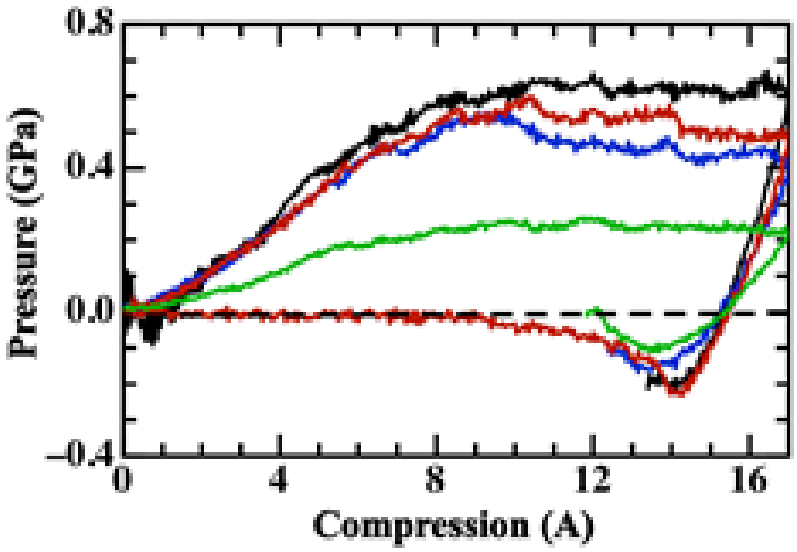

Figure 28: Pressure vs. compression curves for the nanoparticles. Lines show single crystal (black), Janus (blue), Janus with triangular notch (red) and Janus with rectangular notch (green).

Even with no clear fracture events in the pressure VS compression curves, it is useful to examine snapshots of the simulations to determine what mechanisms might underlie the accommodation of the applied stresses. The snapshots for the single crystal NP, the Janus NP, and the Janus with rectangular notch NP in compression are shown respectively in Figure 29, Figure 30, and Figure 31.

Figure 29 shows a slice through the single crystal NP during compression, with the clear appearance of a slip band diagonally across the particle. Although this snapshot only shows the band as it extends over the entire particle, earlier snapshots indicate that this feature began at the bottom of the particle and moved upwards and to the left. The displacement vectors of the individual atoms are also shown in Figure 29. The vectors further indicate that this feature corresponds to slip. This feature began forming at a compression of approximately 5 Å– near where the pressure levels off in Figure 28—and extended across the particle (to the snapshot shown in Figure 29) at approximately 12 Å. The dislocation activity observed during the *in situ* compression of the 0.3 µm particle in the TEM experiment shown in section 3.3 supported the dislocation slip observed here.

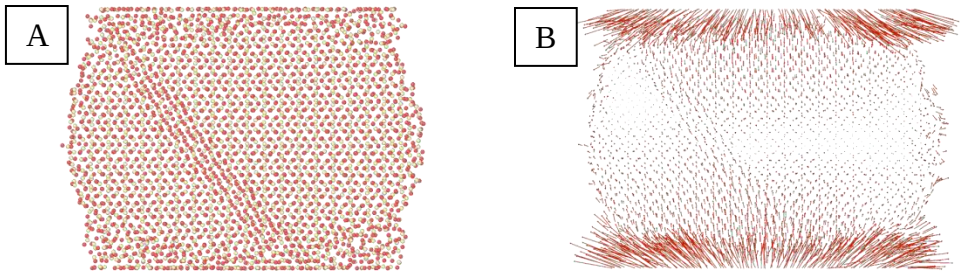

Figure 29: A) Single crystal nanoparticle during compression and B) associated displacement vectors. The feature along the diagonal appears to be a slip plane that has formed.

A snapshot of the compression of the Janus NP after approximately 12 Å and the associated displacement vectors are shown in Figure 30. It is clear from Figure 30 that the original grain boundary has undergone some rotation to the right of the figure, and it is along this pre-existing "defect" that slip occurs. In Figure 28, there is a slight drop in the pressure that corresponds to the beginning of the slip, but it is unclear whether this could be called a fracture event. It is possible that because of the limitations inherent in presenting the total system pressure (as opposed to a true normal force on a compressing platen) the indication of fracture events is different from experiments. Future simulations with atomistic compression plates should clarify this issue.

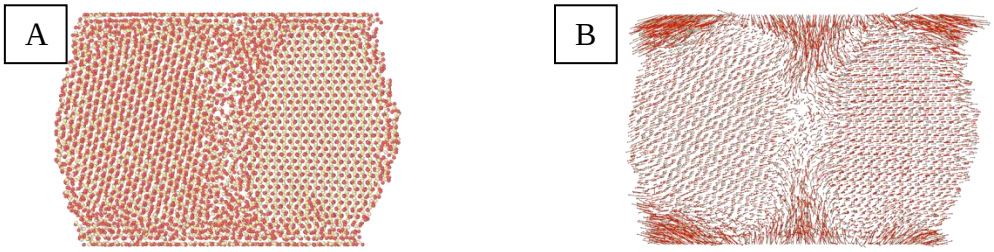

Figure 30: A) Janus nanoparticle under compression and B) associated displacement vectors.

Finally a snapshot of the rectangularly notched Janus NP in compression, with the displacement vectors, is shown in Figure 31. This snapshot, as for the other NPs, corresponds to approximately 12 Å of compression, but the curve in Figure 28 is relatively featureless in this region for this NP. The notch and grain boundary in this case have rotated to the left, but this is a consequence of the compression and disappearance of the notch. The circular patterns seen in the displacement vectors in Figure 31 are related to the overall rotation of the NP itself under compression. We note that this overall rotation was constrained in the single crystal and Janus NPs, but not for the notched NP. It is possible that the lower overall pressures seen in Figure 28 mask any possible pressure drops such as that seen for the unnotched Janus NP.

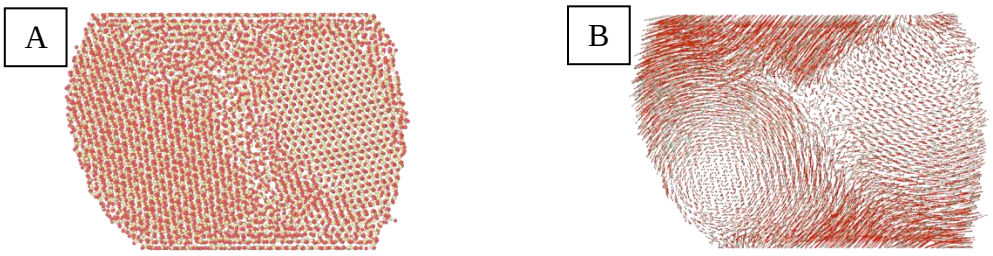

Figure 31: A) Notched nanoparticle under compression and B) associated displacement vectors.

These results indicate that, while a slip plane appears in the single crystal particle, the deformation overall seems to be plastic. There is potentially a fracture event that occurs due to the existence of the grain boundary in the Janus NP, but it is still unclear if this correlates to the type of force drop seen experimentally. Future simulations with better calculations of the normal force can potentially show whether or not this event should be considered a fracture event, and indicate the differences in compression behavior between pre-existing flaws (grain boundaries) and created slip planes.

6. CONCLUSIONS

Particle characterization, using transmission electron microscopy (TEM), showed that the 0.3 μm particles were relatively defect-free single crystals whereas 3.0 μm particles were highly defective single crystals or particles contained low angle grain boundaries. The presence of internal defects and/or internal boundaries plays a role in different deformation behaviors of the sub-micron and micron sized particles in compression. Sub-micron sized particles exhibited ductile deformation whereas micron sized particles exhibited brittle fracture in compression.

The findings from the *in situ* compression experiments supported the atomistic simulation of Al_2O_3 particles in compression. Sub-micron sized Al_2O_3 particles exhibited ductile deformation in compression. *In situ* compression experiments showed 0.3μm particles exhibit significant plastic deformation, before they fractured, and become polycrystalline. Moreover, dislocation activities within the particles were observed during compression. These sub-micron sized Al_2O_3 particles exhibited large accumulated strain before first fracture, 2-3 times that of the micron sized Al_2O_3 particles. The first order approximation of the strain energy release rate of a 0.3μm particle fracturing in compression was G_C = 1,386 J/m^2, a much higher value than bulk Al_2O_3 and other ceramics. This further suggested that the deformation behavior of the sub-micron sized Al_2O_3 particles were much more ductile than normal brittle ceramics.

Atomistic simulation of nano-Al_2O_3 particles showed dislocation slip and significant plastic deformation during compression, in agreement with the findings from experimentation. Simulations of the same sized particles with pre-existing flaws (to mimic the effects of larger particles), however, showed signs of fracture.

Micron sized Al_2O_3 particles exhibited brittle fracture in compression, and *in situ* compression experiments showed that these particles fractured into pieces without observable plastic deformation. Particle deformation behaviors will be used to inform Al_2O_3 coating deposition parameters and particle-particle bonding in the consolidated Al_2O_3 coatings.

7. REFERENCES

1. J. Akedo and H. Ogiso, "Room Temperature Impact Consolidation (RTIC) of Ceramic Fine Powder on Aerosol Deposition," *Journal of Thermal Spray Technology*, 17, 2008, pp. 181-198.

2. J. Akedo. "Room Temperature Impact Consolidation (RTIC) of Fine Ceramic Powder by Aerosol Deposition Method and Applications to Microdevices." *JTTEE5*, 17, 2007, pp. 181-198.

3. J. Akedo, "Aerosol Deposition of Ceramic Thick Films at Room Temperature Densification Mechanism of Ceramic Layers," *J. Am. Ceram. Soc*., Vol. 89, 2006, pp. 1834-1839.

4. Y. Imanaka, N. Hayashi, M. Takenouchi, and J. Akedo, "Technology for Embedding Capacitors on Printed Wiring Board Using Aerosol Deposition," *Proc. of Ceramic Interconnect and Ceramic Microsystems Technologies*, 2006.

5. Y. Imanaka, N. Hayashi, M. Takenouchi, and J. Akedo, "Aerosol Deposition for Post-LTCC," *J. Euro. Ceram. Soc*. Vol. 27, 2007, pp. 2789-2795.

6. Y. Kawakami, H. Yoshikawa, K. Komagata, and J. Akedo, "Powder Preparation for $0.5Pb(Ni_{1/3}Nb_{2/3})O_3$-$0.15PbZrO_3$-$0.35PbTiO_3$ Thick Films by the Aerosol Deposition Method," *J. Crys. Growth*. 275, 2005, el295-el300.

7. J. Akedo and M. Lebedev, "Piezoelectric Properties and Poling Effect of $Pb(Zr, Ti)O_3$ Thick Films Prepared for Microactuators by Aerosol Deposition," *Appl. Phys. Lett*. 77, 2000, p. 1710.

8. S. Sugimoto, T. Maeda, R. Kobayashi, J. Akedo, M. Lebedev, and K. Inomata, "Magnetic Properties of Sm-Fe-N Thick Film Magnets Prepared by the Aerosol Deposition Method," *IEEE Trans. Magnetics.* 39, 2003, pp. 2986-2988.

9. S. Sugimoto, T. Maki, T. Kagotani, J. Akedo, and K. Inomata, "Effect of Applied Field During Aerosol Deposition on the Anisotropy of Sm-Fe-N Thick Films," *J. Magn. Magn. Mater*. 290-291, 2005, pp. 1202-1205.

10. O.A. Ruano, J. Wadsworth, and O.D. Sherby, "Deformation of Fine-Grained Alumina by Grain Boundary Sliding Accomodated by Slip," *Acta Mater*. 51, 2003, pp. 3617-3634.

11. A. Dominguez-Rodriguez, F. Gutierrez-Mora, M. Jimenez-Melendo, J.L. Routbort, and R. Chaim, "Current Understanding of Superplasic Deformation of Y-TZP and Its Application to Joining," *Mater. Sci. Engr. A*. 302, 2001, pp. 154-161.

12. A. Montagne, S. Pathak, X. Maeder, and J. Michler, "Plasticity and fracture of sapphire at room temperature: load-controlled microcompression of four different orientations," *Ceram Int* 40, 2014, pp. 2083-2090.

13. J. Deneen, W.M. Mook, A. Minor, W.W. Gerberich, and C.B. Carter, "In situ deformation of silicon nanospheres," *J Mater Sci* 41, 2006, pp. 4477-4483.

14. W.W. Gerberich, W.M. Mook, M.J. Cordill, C.B. Carter, C.R. Perrey, J.V. Heberlein, and S.L. Girshick, "Reverse plasticity in single crystal silicon nanospheres," *Int J Plasticity* 21, 2005, pp. 2391-2405.

15. F. Ostlund, K. Rzepiejewska-Malyska, K. Leifer, L.M. Hale, Y. Tang, R. Ballarini, W.W. Gerberich, and J. Michler, "Brittle-to-Ductile Transition in Uniaxial Compression of Silicon Pillars at Room Temperature," *Adv. Funct. Mater*. 19, 2009, pp. 2439-2444.

16. V. Swamy, A. Kuznetzov, L.S. Dubrovinsky, P.F. McMillan, V.B. Prakapenka, G. Shen, and B.C. Muddle, "Size-Dependent Pressure-Induced Amorphization in Nanoscale TiO_2," *Phys. Rev. Lett*. 96, 2006, pp. 135702-4.

17. M. Chen, J.W. McCauley, and K.J. Hemker, "Shock-Induced Localized Amorphization in Boron Carbide," *Science*, 299, 2003, pp. 1563-1566.

18. G. Subhash, S. Maiti, P.H. Geubelle, and D. Ghosh, "Recent Advances in Dynamic Indentation Fracture, Impact Damage and Fragmentation of Ceramics," *J. Am. Ceram. Soc*. 91, 2008, pp. 2777-2791.

19. A.L. Sanchez, J.A. Hubbard, J.G. Dellinger, and B.L. Servantes, "Experimental Study of Electrostatic Aerosol Filtration at Moderate Filter Face Velocity," *Aerosol Science and Technology*, vol. 47, 2013, pp. 606-615.

20. K. Hattar, D.C. Bufford, and D.L. Buller, "Concurrent in situ ion irradiation transmission electron microscope*," Nuclear Instruments and Methods in Physics Research B.* 338, 2014, pp. 56–65

21. W.M. Mook, J.D. Nowak, C.R. Perry, C.B. Carter, R. Mukherjee, S.L. Girshick, P.H. McMurry, and W.W. Gerberich, *Phys Rev B*, 75, 2007, pp. 214112-1-10.

22.Accuratus Corporation (2014) Aluminum Oxide, Al_2O_3 Ceramic Properties. http://accuratus.com/alumox.html. Accessed 9/5/2014.

23. Y. Chen, R.E. Palmer, and J.P. Wilcoxon, "Sintering of passivated gold nanoparticles under the electron beam," *Langmuir*, 22, 2006, pp. 2851-2855.

24. Hysitron I (2013) SEM Picoindenter User Manual. Revision 9.3.0913 edn.,

25. S. Blonski and S.H. Garofalini, "Molecular Dynamics Study of Silica-Alumina Interfaces," *J. Phys. Chem*. 100, 1996, pp. 2201-2205.

26. D.A. Litton and S.H. Garofalini, "Modeling of Hydrophilic Wafer Bonding by Molecular Dynamics Simulations," *J. Appl. Phys*. 89, 2001, pp. 6013-6023.

27. J.-M. Delaye and D. Ghaleb, *Phys. Rev*. B 61, 2000, pp. 14481-14493.

DISTRIBUTION

1	MS0886	Paul Kotula	01819
1	MS0886	Bonnie McKenzie	01819
1	MS0889	Michael Chandross	01814
1	MS0889	Jay Carroll	01831
1	MS0889	Brad Boyce	01831
1	MS0959	Deidre Hirschfeld	01832
1	MS1056	Daniel Bufford	01111
1	MS1130	Aaron Hall	01832
1	MS1130	Pylin Sarobol	01832
1	MS1123	David Urrea	01832
1	MS1304	William Mook	01132
1	MS0899	Technical Library	09536 (electronic copy)

Sandia National Laboratories